# Eberhard Karls Universität Tübingen
Mathematisch-Naturwissenschaftliche Fakultät
Wilhelm-Schickard-Institut für Informatik

# Bachelor Thesis Informatics

## Evolution of ENSO precipitation teleconnections

Alexej Onken

3rd March 2022

**Reviewer**

Dr. Bedartha Goswami
Machine Learning in Climate Science
Cluster of Excellence "Machine Learning"
University of Tübingen

# Acknowledgments

I would like to thank my supervisor Dr. Bedartha Goswami for the excellent support and familiarization with the topic. My thanks also go to the entire MLCS group for the useful food for thought and creative discussions related to the project. The interesting topic helped me to dive into the exciting world of climate science and discover the useful contribution of machine learning.

# Selbständigkeitserklärung

Hiermit versichere ich, dass ich die vorliegende Bachelorarbeit selbständig und nur mit den angegebenen Hilfsmitteln angefertigt habe und dass alle Stellen, die dem Wortlaut oder dem Sinne nach anderen Werken entnommen sind, durch Angaben von Quellen als Entlehnung kenntlich gemacht worden sind. Diese Bachelorarbeit wurde in gleicher oder ähnlicher Form in keinem anderen Studiengang als Prüfungsleistung vorgelegt.

Ort, Datum                                                    Unterschrift

# Evolution of ENSO precipitation teleconnections

**Alexej Onken**[a]**, Bedartha Goswami**[a]

[a]University of Tuebingen, Machine Learning in Climate Science, Cluster of Excellence "Machine Learning", Maria-von-Linden-Str. 6, Tuebingen, Germany, 72076

**Abstract.** The El Niño Southern Oscillation (ENSO) is one of the most important climate phenomena on our planet. It affects precipitation globally through aperiodic changes in ocean currents triggered by sea surface temperatures (SSTs) in the equatorial Pacific Ocean. To measure the global impact of ENSO on rainfall, several methods are used, such as correlation analyses. Cross-correlation analyses are typically used to identify linear relationships and their time lags to evaluate teleconnection links. However, standard correlation analyses can produce spurious teleconnections due to indirect links, common drivers, or autocorrelations, biasing interpretability, thus making cause-effect relationships difficult to establish. Moreover, little is known about the extent to which teleconnection maps have changed over the past several decades. Here, in addition to standard correlation analysis, we use the PCMCI+CEN causal discovery approach to reveal the effects of a range of El Niño SST indices on global precipitation amounts across multiple time window to better understand the uniqueness of each ENSO region. By removing confounding effects of different Niño regions on the index regions under analysis, we identified causal relationships with lags of up to 12 months that describe the unique impacts of individual Niño regions. Furthermore, trends in spatial correlation fields between the Oceanic Niño Index (ONI) from the tropical Pacific El Niño region and global precipitation anomalies were determined for lag 0 and quantified with 10-year sliding time windows. The Maritime Continent Region and the Southwest Pacific Region, which are the largest regions anticorrelating with ENSO, showed a waning trend, while the largest positively correlating Central Pacific Region showed only slight fluctuations until 2012, after which a slight decreasing trend was observed. We found that cross-correlation analyses for all El Niño SST indices (Niño 1+2, 3, 4, ONI) for teleconnections at lag -1 (month) yielded the most significant hits (in terms of modes and medians), which are indicative of strong correlations. Causal maps created using the PCMCI+CEN approach partially corroborate ENSO's previous knowledge of teleconnection maps, but other regions allegedly influenced by ENSO are poorly covered or in some cases not masked at all. Our results demonstrate that although different El Niño SST indices are strongly intercorrelated, regions can be identified that represent very unique characteristics of ENSO events. We expect that our work will help to understand how driving forces in the form of univariate time series can affect the climate in the regions studied, such that expert knowledge can be used to better understand the causes of local influences on climate variables such as temperature, precipitation, or atmospheric pressure. Sliding time windows for correlation analyses or causal map analyses can help assess the extent to which anthropogenic climate change may have played a role in changes in global teleconnections over recent years or decades.

**Keywords:** El Niño Southern Oscillation, Correlation analysis, Correlation map, Causal discovery algorithm, PCMCI algorithm, Causal map, Global precipitation teleconnections, Causal Effect Networks, Oceanic Niño Index.

**Correspondence**: Alexej Onken  alexej.onken@student.uni-tuebingen.de

# 1 Introduction

The El Niño-Southern Oscillation (ENSO) is known for many rainfall patterns around the world. Countries bordering the Pacific Ocean are particularly affected. These include notably South America, but also Southeast Asia and the United States. It becomes problematic when major floods or droughts threaten human lives. As a result, the local population suffers greatly and humanitarian disasters can occur, such as dwindling fish stocks due to reduced upwelling on the Peruvian coast (Dante Espinoza-Morriberon et al., 2017). Due to the effects of ENSO on the Walker circulation, which involves shifts in jet streams, regional but also global changes in weather patterns are observed. The influences of ENSO on the Walker circulation are widely understood and can be observed accordingly during extreme weather events such as off the coasts of Indonesia or South America. In this context, teleconnections offer a solid way to form links between weather processes in the tropical Pacific and other remote areas. This may help to ensure that institutional preparations are made in affected regions to prevent worse damage in the future, in addition to measures to slow human-induced climate change.

There are several regions in the equatorial Pacific where regionally averaged SST anomalies are tracked that are related to ENSO and the associated shift in the Walker circulation. The so-called Niño 3.4 (5N-5S, 170W-120W) is the most common of all regions and is used, among other things, to calculate the Oceanic Niño Index (ONI), which describes the state of ENSO. However, such Central Pacific El Niños (CPs) do not correspond to the traditionally assumed origin of ENSO, which is in the Niño 1+2 region (0-10S, 90W-80W) (Trenberth et al., 2001). This region is the smallest and most easterly of all the regions used to describe ENSO, and was recognized as such by local populations in earlier times (Trenberth et al., 2001). These traditional eastern Pacific El Niños (EPs) differ from CPs in that during CPs the Niño 1+2 region is not necessarily affected by SST anomalies (Kao et al., 2008). Other regions that describe ENSO phenomena are the Niño 3 (5N-5S, 150W-90W) and Niño 4 (5N-5S, 160E-150W) regions. Previously, it was assumed that the Niño 3 region was capable of robustly predicting ENSO. However, it was later learned that ENSO interdependencies between the ocean and atmosphere lie further west (Trenberth, NCAR, 2016). As a result, Niño 3 was gradually replaced by ONI (Niño 3.4 region).

The Niño 4 region is the westernmost of all regions and describes the SSTs in the equatorial Central Pacific. Figure 1 shows the ENSO SST anomaly regions at a glance. Another interesting index that describes the unique nature of the ENSO event is the Trans-Niño Index (TNI). The TNI is calculated from the difference in normalized SST irregularities (anomalies) between the Niño 1+2 and Niño 4 regions. Moreover, the ONI (Niño 3.4 region) can be considered approximately as the sum of Niño 1+2 and Niño 4 regions, where ONI and TNI are approximately orthogonal (weakly correlated) to each other at zero lag (Trenberth et al., 2001).

Nevertheless, it is not clear how precipitation patterns have evolved in recent decades and what the projections for the future will be. Also, not enough is known about the various influences of the individual Nino regions or which SST regions in the Central Pacific are causing which precipitation anomalies on a global scale. While there are studies that refer to correlation analyses and also consider time lags, these feature only seasonal analyses, and refer to simulation data (Haszpra et al., 2019). Here we try to analyze observational data and extend the analysis to the whole year. In this way, we can observe the behavior of the last decades and look at the changes of individual regions with the help of sliding windows. However, correlation analyses ignore autocorrelations, indirect links, and common driver effects that can hide true cause-and-effect relationships in the

background (Kretschmer et al., 2016; DiCapua et al., 2020). Therefore, we extend our analysis with the PCMCI+CEN (Runge et al. 2020; DiCapua et al., 2020) tool to make causal statements about the influences of the Niño regions from Figure 1. The PCMCI algorithm is an extension of the PC algorithm (Spirtes et al., 2000) that allows us to create causal impact networks (CENs) (Kretschmer et al., 2016) by applying standardized multiple regression so that causal influences of causal time series can be quantified and visualized on a spatial map. The goal of this paper is to show how these methods (correlation analysis and PCMCI+CEN) can be applied to verify or challenge existing knowledge about ENSO teleconnections.

This manuscript is organized as follows: Section 2 describes the origin and processing methods of the data required for the analyses. Section 3 explains the methods used, which include the setup of the correlation analysis, but also a step-by-step description of the PCMCI+CEN algorithm. Section 4 addresses the main findings of the correlation analysis as well as PCMCI+CEN. The correlation analysis considers the case of instantenous correlations of ONI with global time series of precipitation anomalies, as well as correlations in which the Niño regions (1+2, 3, 4 and ONI) are leading in time. In PCMCI+CEN, we look at Niño regions as well as their leading lags in the first part to highlight precipitation anomalies worldwide. In the second part, we consider and eliminate the influences of other regions. All results from all analyses are checked for consistency with the teleconnections from Figure 2. We then address the challenges and limitations of the analyses, as well as further recommendations. Finally, in Section 5, we summarize the main findings and take a brief look into the future in the context of the results.
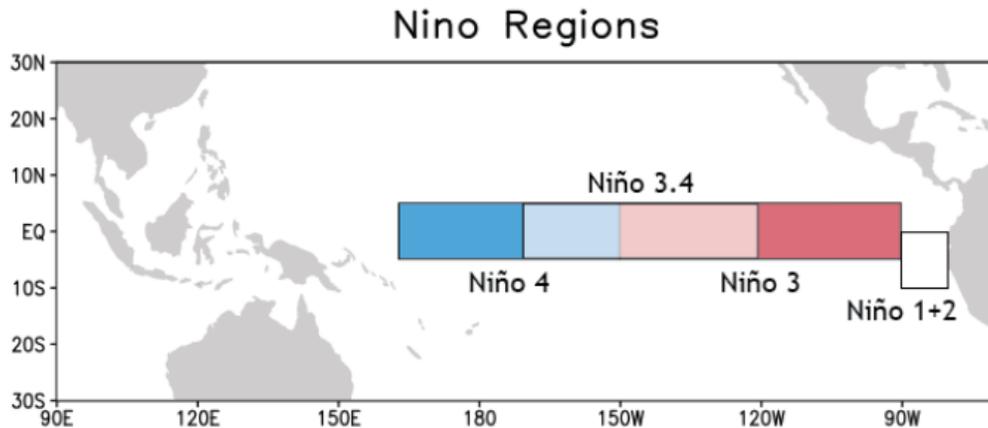


Fig 1: ENSO Central Pacific Regions. (source: www.climate.gov, last access: 26 December 2021)

## 2 Data

To capture the influences of ENSO actors on precipitation anomalies, we must first make a judicious selection of the univariate time series to be considered. Indeed, there are a number of ENSO indicators. These include the Southern Oscillation Index (SOI) between Tahiti and Darwin, Outgoing Longwave Radiation (ORL), equatorial Pacific sea surface temperatures (SSTs), and multivariate combinations of the above variables (National Oceanic and Atmospheric Administration, 2021, Indicators). We limit our analysis to SSTs in the equatorial Pacific as the ENSO

regions and associated teleconnections are of interest to us, not least because the mutual interaction between the Pacific Ocean and the Walker circulation seems most plausible from the relevant literature. Moreover, we take global 3D (latitude, longitude, time) precipitation data, with each geographic location representing a univariate time series.

For our analysis, we use the National Oceanic and Atmospheric Administration (NOAA) monthly GPCP precipitation dataset (data can be found under https://psl.noaa.gov/data/gridded/data.gpcp.html, last access: 01 December 2021) for the period from January 1979-March 2021 (2.5° x 2.5°). The dataset combines rain gauge stations, observations, and satellite data on a global grid with a total of 144 x 72 = 10368 points. For each grid point in the monthly GPCP precipitation data, we calculate climatological anomalies for the period 1981-2010 by computing the long-term average for each month and subtracting it from the GPCP dataset. Because the PCMCI+CEN algorithm requires stationary time series, we remove linear trends in the precipitation anomalies. The period January 1979-March 2021 is used for the correlation analysis, while in the PCMCI+CEN analysis we consider the interval between January 1982-March 2021.

To capture different ENSO states for both the correlation analysis and the PCMCI+CEN approach, we use, inter alia, NOAA's monthly Niño 3.4 index. The Niño 3.4 region (5N-5S, 170W-120W) is then used to calculate the ONI (data can be found under https://origin.cpc.ncep.noaa.gov/products/analysis_monitoring/ensostuff/ONI_change.shtml, last access: 01 December 2021). Based on a warming trend in the Niño-3.4 region since 1950, NOAA's Climate Prediction Center (CPC) adjusts fixed 30-year climatological base periods. Using these multiple 30-year base periods, deviations from averages (anomalies) are determined and updated every 5 years (1936-1965, 1941-1970,...,1991-2020). These measures are used to reflect the inter-annual variability of ENSO. We then calculate a 3-month running mean using the adjusted 30-year base periods and associated ERSST.v5 SST anomalies. We take the other monthly OISST.v2 Niño indices (Niño 1+2, 3, 4) with the climatological base period 1991-2020 from NOAA, and also calculate a 3-month running mean of the SST anomalies for the periods 1982-2021. The data can be found here https://www.cpc.ncep.noaa.gov/data/indices/sstoi.indices, last access: 01 December 2021.

To determine the Trans-Niño Index (TNI), we normalize the time series of Niño 1+2 and Niño 4, and then subtract the normalized version of Niño 4 from the normalized one of Niño 1+2. Normalization here means that we subtract the mean from each data point in the two time series, and then divide the numerator by the standard deviation.

## 3 Methods

For the following methods and preprocessing of the data, we use the free and publicly available Relational Database Management System (RDBMS) PostgreSQL. The Structured Query Language (SQL) combined with Turing completeness is intuitive and elegant for merging, filtering, and grouping tabular data. PostgreSQL is largely compliant with current SQL standards, among other things we use the recursive query option as well as the window functions. Using Python and the Basemap toolkit, we visualize the results on a world map. The computations of the PCMCI+CEN algorithm were performed using the causal time series analysis Python package called Tigramite by Jakob Runge, which is freely available on https://github.com/jakobrunge/tigramite/blob/master/README.md. The corresponding source code and all plots are also available on GitHub https://github.com/jexela/mlcs_el_ni-o_analysis.

### 3.1 Correlation Analysis

Correlation analysis can be used to determine statistical relationships between two variables. We restrict our analysis to the dimensionless Pearson Correlation Coefficient (PCC), which describes the linear two-way relationship between ENSO indices (Niño 1+2, 3, 4, ONI) and precipitation anomalies. Statistically significant relationships are flagged and visualized on a teleconnection map. We do not limit our analysis to seasonal precipitation, but consider all months in our analysis. In the first part, we examine the ONI from the Niño 3.4 region and calculate the correlation coefficients without lags for 10-year time windows, starting with 1979-1988, 1980-1980,..., 2012-2021. In addition, we quantify the largest shapes in the spatial correlation fields and calculate their approximate areas for each time window. In the second part of the correlation analysis, we consider the other Niño regions in addition to ONI, but this time only with time lags. Since we assume ENSO to be the cause of departures from normal precipitation, the ENSO indices are time-lagged, i.e., they range from $\tau_{min} = -1$ to $\tau_{max} = -12$ (month). Next, we mark the medians and modes of the time lags in the spatial fields for each ENSO index. In the next two subsections, we turn to the details of the correlation analyses.

#### 3.1.1 Correlation Analysis Part 1

In the first part of the correlation analysis, we restrict ourselves exclusively to the ONI (Niño 3.4 region). We then proceed as follows: Each world point is divided into time windows consisting of intervals of the form $[T - W, T]$ that continue from year to year. The variable $W$ is representative of the length of the window, while $T$ is the end time of the window. Moreover, time windows are constructed with $W = 9$ (10-year time window), for the first time window $T_{first} = 1988$ and the last time window $T_{last} = 2021$. Thus, the first interval is $[1979, 1988]$, the second is $[1980, 1989]$ and so on. The last interval is $[2012, 2021]$ and extends only to March 2021, resulting in a shortening of the data points by 9 months (111 months in total). All other intervals have a size of 10 years and accordingly contain 120 data points (120 months). For each data point at each grid point (10368 grid points in total), the precipitation anomaly (climatology 1981-2010) for that time (year,month) is documented, as well as the current ONI index (no time lags). Using this information, Pearson's correlation coefficients can be calculated for all data points and grid points within the above 33 time windows. For a significance level of $\alpha = 0.05$, we subsequently calculate the $p$-values of the PCCs using a $t$-distribution approximation as defined by Zogheib and Elsaheli (2015). To evade the problem of multiple testing, we employ a false discovery rate (FDR) control method (Benjamini and Hochberg, 1995). All significant hits are subsequently visualized for all 33 time windows on a correlation map. Using the recursive query option, we calculate the largest approximately contiguous correlated area as well as the largest anticorrelated area for each time window. After identifying the grid points belonging to the largest areas, considering the largest correlating area and the largest anticorrelating area individually, we calculate their area using the great circle distance method. The corresponding areas of the respective points are then summed up, in the course of which the total areas of the two largest areas can be quantified.

#### 3.1.2 Correlation Analysis Part 2

As we expect that ENSO indices to be the cause of precipitation anomalies, we perform correlation analyses where ENSO indices (Niño 1+2, 3, 4, ONI) precede in time. In this part of the analysis, we retain 31 (starting from 1982) of the 34 time windows from the first part of the analysis and

calculate the correlation coefficients between ENSO indices and precipitation anomalies for each time lag. In this study we focus on a time lag range of $\tau_{min} = -1$ to $\tau_{max} = -12$ (month). The minus sign means that the ENSO index under consideration is leading in time. To put it concisely, we calculate the correlation coefficients for each grid point, in each time window at each time lag. To investigate which ENSO time lags are prevalent at which grid point, we must first determine which time lag represents the maximum absolute correlation in that particular time window. Using the distributions of the dominant time lags across each of the 31 time windows, we mark the medians and modes (time lags that appear most often) for each grid point. Problematically, confidence intervals around the PCCs are not symmetric and therefore not approximately normally distributed. Therefore, we perform a Fisher z-transformation (Banik et al., 2016) to mimic a normal distribution. The transformed correlation values can be seen as a cross-correlation function. The high peaks of the cross correlation function represent those strong correlations that are at least two standard deviation away from the mean in that particular window. This is a type of filter to distinguish strong correlations from noise. If the dominant time lag does not meet this requirement, no significant time lag is noted for that particular window. Further filters are a small interquartile range for the medians, a certain number of occupied windows with dominant time lags for a grid point and a mask for the absolute size of the correlation. Grid points that meet these requirements are marked and visualized accordingly.

### 3.2 *PCMCI and Causal Effect Networks*

To better understand the causal relationships between the different Niño variables and precipitation anomalies, we use the PCMCI causal detection tool following (Runge et al., 2019). The main goal of PCMCI+CEN is to detect and remove spurious correlations when controlling for one or more variables. One of the prerequisites for this is the careful selection of potential drivers, which requires expert knowledge. When considering ENSO influences on global precipitation anomalies, ENSO regions offer themselves as possible influencers.

The PCMCI+CEN algorithm for causality detection consists of 3 steps. The first step is the so-called PC (named after its authors Peter Spirtes and Clark Glymour) algorithm (Spirtes et al., 2001), in which partial correlations are used to successively eliminate influences of common drivers and indirect links. In this process, a first set of potential parents is estimated, with only significant partial correlations considered in each step for each number of conditions. In the second step, called Momentary Conditional Independence (MCI), additional autocorrelations are detected to identify a final set of parents. Again, only significant partial correlations are considered, using the set of preliminary parents as the test for each actor. In the third step, Causal Effect Networks (CENs) (Kretschmer et al., 2016; Di Capua et al., 2020) are estimated for each 2D point $F(lat, lon)$ (representative for precipitation anomalies) using standardized multiple regression. This allows quantification of the causal effects of the different Niño regions on $F(lat, lon)$. On account of the standardized regression coefficients, it can be shown how strongly the independent variables (Niño indices) incite variability in the dependent variable $F(lat, lon)$. CENs can be understood as directed graphs describing the relationship between a 3D (lat,lon,time) climate data set and a 1D time series (actors). Thus, each individual grid point and the corresponding time series of the precipitation anomaly $F(lat, lon)$ has exactly one associated CEN. These CENs, similar to the correlation maps, can be represented as spatial shapes on a world map. The direction of the arrows reflects the causal relationship between the actor and the climate data grid point.

In our analysis, we also consider instantaneous relationships where, strictly speaking, no causal relationships can be established. Such an edge would of course have no direction in the underlying graph. Nevertheless, we assume that the SSTs in the equatorial Pacific are more likely to be the cause of the precipitation anomalies, rather than the other way around. At higher temporal resolution, these could possibly be confirmed as well (e.g., $\tau = -15$ (days)), but we limit ourselves to $\tau_{min} = -1$ (month). It should be pointed out that the use of PCMCI is based on certain assumptions (Runge et al., 2019). The use of partial correlations to test conditional independence of two variables requires, among other things, stationarity and linearity of the potential link. The following explains how to apply the PCMCI+CEN. All multiple testing problems in the PCMCI+CEN procedure were handled with the FDR correction (Benjamini and Hochberg, 1995).

*Step 1 (PC Algorithm): Estimate preliminary set of parents*

For a given significance level (e.g. $\alpha = 0.05$), we need to determine for each actor, i.e., for a univariate time series, the causal parents that can be considered as the source of the incoming links in the CENs. For this we consider the time series $A, B, C, D, E, F(lat, lon)$. The set of actors $\{A, B, C, D, E\}$ are the different ENSO indices (Niño 1+2, 3, 4, ONI, and TNI). For these time series it is now necessary to look at the past, i.e. $\{A_{\tau=-1,}, B_{\tau=-1,}, ..., F(lat, lon)_{\tau=-1,}, ..., A_{\tau=-\tau_{max}}, B_{\tau=-\tau_{max}}, ..., F(lat, lon)_{\tau=-\tau_{max}}\}$. An example is shown below for illustration purposes:

In the first iteration phase of the PC algorithm, the correlation between the actor under consideration (e.g., $A$) and all other actors (including the past of $A$ itself) at different time lags is determined. Since the influence of one or more other variables has not been eliminated in the first iteration, it is a zero-order partial correlation. Thus, a zero-order partial correlation is the correlation coefficient (PCC) between two variables. Let $\rho$ denote the partial correlation coefficient and let $\nu$ denote the number of conditions. In the first iteration phase we get a first set of preliminary parents $\mathcal{P}_A^{\nu=0}$ for actor $A$:

- $\nu = 0, \alpha = 0.05$

    - $\rho(A_{\tau=0}, A_{\tau=-1}), ..., \rho(A_{\tau=0}, A_{\tau=-12})$
      $\rho(A_{\tau=0}, B_{\tau=-1}), ..., \rho(A_{\tau=0}, B_{\tau=-12})$
      $$\vdots$$
      $\rho(A_{\tau=0}, F(lat, lon)_{\tau=-1}), ..., \rho(A_{\tau=0}, F(lat, lon)_{\tau=-12})$
    - $\mathcal{P}_{A_{\tau=0}}^0 = \{A_{\tau=-2}, B_{\tau=-1}, C_{\tau=-5}, F(lat, lon)_{\tau=-2}\}$

Please note that the preliminary parent set $\mathcal{P}_A^0$ is selected arbitrarily. Only significantly correlated ($\alpha = 0.05$) time-lagged actors end up in $\mathcal{P}_A^0$. In the next iteration step $\nu = 1$, we start conditioning on variables from $\mathcal{P}_A^0$:

- $\nu = 1, \alpha = 0.05$

    - $\rho(A_{\tau=0}, B_{\tau=-1}|A_{\tau=-2}), ..., \rho(A_{\tau=0}, F(lat, lon)_{\tau=-2}|A_{\tau=-2})$
      $\rho(A_{\tau=0}, A_{\tau=-2})|B_{\tau=-1}), ..., \rho(A_{\tau=0}, F(lat, lon)_{\tau=-2}|B_{\tau=-1})$
      $$\vdots$$
      $\rho(A_{\tau=0}, A_{\tau=-2})|F(lat, lon)_{\tau=-1}), ..., \rho(A_{\tau=0}, C_{\tau=-5})|F(lat, lon)_{\tau=-12})$
    - $\mathcal{P}_{A_{\tau=0}}^1 = \{A_{\tau=-2}, B_{\tau=-1}, F(lat, lon)_{\tau=-2}\}$

7

Again, only significant parents survive and enter $\mathcal{P}_A^1$. In the next step $\nu = 2$, we would then condition on two processes, but this time from $\mathcal{P}_A^1$. Some correlations between $A$ and actors from $\mathcal{P}_A^1$ could have arisen from multivariate influences. This process continues until the algorithm converges so that $\nu$ cannot be increased any further. For example, $\mathcal{P}_{A_{\tau=0}}^{\nu=\nu_{conv}} = \{A_{\tau=-2}, B_{\tau=-1}\}$ would then be the converged preliminary set of the PC step for actor $A$. This process must of course be repeated for all other time series $B, C, D, E$ and each associated $F(lat, lon)$ to obtain the corresponding preliminary parent sets $\{\mathcal{P}_{A_{\tau=0}}^{\nu=\nu_{conv}}, \mathcal{P}_{B_{\tau=0}}^{\nu=\nu_{conv}}, \mathcal{P}_{C_{\tau=0}}^{\nu=\nu_{conv}}, \mathcal{P}_{D_{\tau=0}}^{\nu=\nu_{conv}}, \mathcal{P}_{E_{\tau=0}}^{\nu=\nu_{conv}}, \mathcal{P}_{F_{\tau=0}(lat,lon)}^{\nu=\nu_{conv}}\}$. The parents $A, B, C, D, E$ are strictly tied to the parents of $F(lat, lon)$, which means that the preliminary parents must be calculated for each longitude and latitude position (6 preliminary parent sets per position).

*Step 2 (MCI): Estimate edge strength by removing autocorrelations*
In the MCI step, the influence strength of the potential incoming connections is determined. Again, all possible combinations of partial correlations between actors and time-lagged counterparts are considered. In contrast to the PC step, both input processes are conditioned upon. In doing so, the preliminary parents from the PC step are conditioned out for the non-time-lagged input process. The additional conditioning is also done for the time-lagged actor, which helps to account for autocorrelations. Now to inspect if $X_{\tau=-j} \to Y_{\tau=0}$ for $j \in \{0, ..., \tau_{max}\}$ holds, MCI checks:

$$\rho(X_{\tau=-j}, Y_{\tau=0} | \mathcal{P}_{X_{\tau=-j}}, \mathcal{P}_{Y_{\tau=0}})$$

Those parents that survive this testing procedure to a certain level of significance (e.g., $\alpha = 0.05$) form the final set of causal parents for that actor $Y_{\tau=0}$. Accordingly, the MCI test procedure performs a false positive assessment for interdependent time series (Runge et al., 2019), which is the case in the Niño-SST regions.

*Step 3: Construct CENs with standardized linear regression*
Last but not least, CENs are constructed using the final causal set of parents from PCMCI (Di Capua et al., 2020), which form the independent variables of a standardized multiple regression for each actor (dependent variable). Each grid point has its own CEN containing all processes $A, B, C, D, E, F(lat, lon)$ as nodes and the directed causal relations with the corresponding time lags as edges:

$$Y_{\tau=0} = \sum_{j=1} \beta_j X^j + \epsilon_{Y_{\tau=0}}$$

where $Y_{\tau=0} \in \{A, B, C, D, E, F(lat, lon)\}$ is the dependent variable, $j \in \{1, ..., N\}$, $X^j \in \mathcal{P}_{Y_{\tau=0}}$ is the set of $N$ independent variables (causal parents) belonging to $Y_{\tau=0}$, and $\epsilon_{Y_{\tau=0}}$ is the residual. The regression coefficients $\beta_j$ can then be used to create causal maps. Causally, $X_{\tau=-i}^j \to Y_{\tau=0}$ for $i \in \{0, ..., \tau_{max}\}$ means that if $X_{\tau=-i}^j$ increases by one standard deviation (ceteris paribus), $Y_{\tau=0}$ increases by $\beta_j$ standard deviations.

In our analysis, we restrict ourselves exclusively to the causal parents of $F(lat, lon)$. Of course, several time lags of a Niño variable (e.g. ONI) can be causal parents of $F(lat, lon)$. In order to be able to map them nevertheless on a causal map, we take in each case the largest absolute regression coefficients (lag 0-12 & 1-12) of the Niño causal variable.
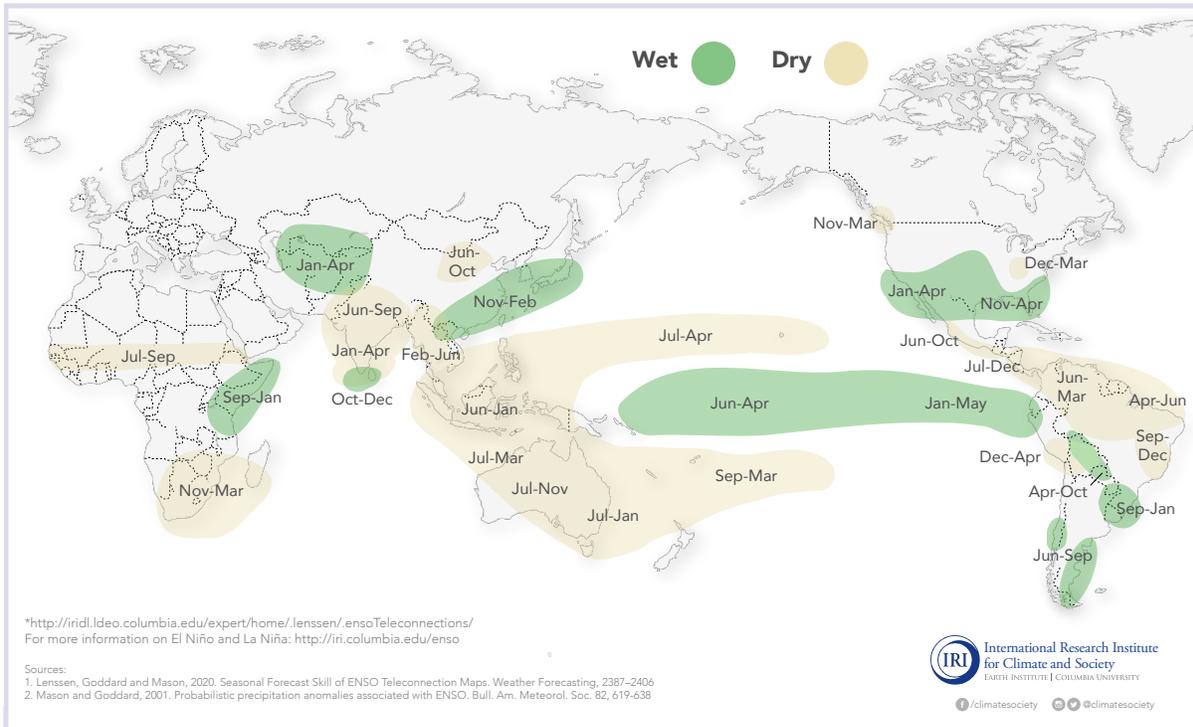
Fig 2: Basemap for ENSO teleconnections (El Niño case). This map is used to compare the results of the correlation analysis and the PCMCI+CEN algorithm. (source: https://iridl.ldeo.columbia.edu/maproom/IFRC/FIC/elninorain.html, last access: 26 December 2021)

## 4 Results and discussion

To compare our findings with the relevant literature, we refer to the ENSO teleconnection maps from the International Research Institute for Climate and Society (IRI) in Figure 2. Here, green areas representing wet periods are accompanied by positive Niño indices. Positive Niño indices observed over several months represent El Niño phases, while negative Niño indices denote La Niña episodes. Figure 2 explicitly describes the relationship between El Niño and precipitation. Similarly, there is also a map of La Niña teleconnections (available at https://iridl.ldeo.columbia.edu/maproom/IFRC/FIC/laninarain.html, last access: 26 December 2021) showing similar areas (in terms of location and shape) as Figure 2, with correspondingly reversed meanings (green areas represent negative Niño indices and vice versa). Note that Figure 2 refers to specific seasons or monthly intervals. In our analyses, however, we consider all months over several years, not least because the PCMCI+CEN approach requires many data points to train. Seasonal analyses with multiple sliding windows would be a study in themselves, as some regions are exclusively susceptible to equatorial Pacific SST anomalies in certain months.

### 4.1 Correlation Analysis

### 4.1.1 Correlation Analysis Part 1

Figure 3 shows the time evolution of the spatial correlation fields of the two largest correlating and anticorrelating regions. Here, 1984 refers to the total areas of the 10-year window [1979, 1988], 1985 to [1980, 1989], and so on to 2017, which is the final window [2012, 2021]. This analysis is restricted to ONI only, without lag. The time windows with the largest (1984) and smallest extent (2017) of the largest anticorrelating areas are shown in Figures 4 (left) and 5 (right). Also, two local minima of the largest blue area (1991, 2005) are shown in Figures 4 (right) and 5 (left). Each of the time windows has a threshold value $|r_{min}|$ that represents the smallest significant $p$-value after applying the Benjamini-Hochberg method. The largest correlating red area is overall more stable than the largest blue area and therefore has a lower elongation. In addition, a similar frequency can be seen without much phase shift, suggesting that local extreme points (minimum or maximum extent of the areas) of red and blue often coincide, as in the 1991, 1996, 2007, and 2017 windows. The remaining windows can be found on GitHub https://github.com/jexela/mlcs_el_ni-o_analysis.

The biggest blue-coloured anticorrelating region mainly includes the Maritime Continent and the southwestern Pacific, but also partially extends to the southern Pacific. The maximum extent of the largest anticorrelating area is in the 1984 time window and is $11,757,936$ $km^2$, the minimum is in the last time window 2017 with $2,931,376$ $km^2$, while the average area from all time windows is $7,684,786$ $km^2$. In none of the 34 windows does a blue contiguous connection (and thus area) exist between the Maritime Continent, the southern (or southwestern) Pacific, and the northern Pacific, as shown in Figure 2. The droughts in the northern Pacific, which are fixed to the July-April period (10 months) in the El Niño case in Figure 2, occur only in the Nino 3.4 longitudes (170W-120W) in our analysis. The Australian mainland was barely covered by the largest blue area except in 5 windows during 1996-2011. This could be attributed to the fact that the anticorrelating influence (and thus droughts) of ENSO is particularly strong over the Australian mainland during the cold seasons in the southern hemisphere (July-November, 5 months), see Figure 2. Since 1990, at least one Australian coastal region has been touched by the largest blue area.

Other regions that are consistently anticorrelated in all 34 windows are the northern part of South America, particularly the northern part of Brazil (Amazon region). This is consistent with the teleconnection map in Figure 2 as it predicts drought for El Niño or precipitation patterns for La Niña almost consistently throughout the year (June-March, 10 months). It should also be emphasized that the Darién Gap has been repeatedly affected by droughts related to El Niño. This is in harmony with Figure 2. Nevertheless, there is not always a direct link between the northern Brazilian area and the Darién Gap. Since 1988, most of the Colombian coast has also been affected by droughts. The west coast of Central America also does not show evidence of droughts as in Figure 2. This could be due to the seasonal nature (June-October, 5 months). Interestingly, in the time windows covering the period 1998-2007, droughts are visible at the southernmost tip of South America that are related to El Niño. These are not visible in Figure 2. The greatest extent is seen in the 1990-1999 time window.

In the time windows covering the period 1979 to 2009, the southeastern African continent tends to be affected by droughts associated with El Niño. This appears in accordance with Figure 2, although the intervals from 2010 onward no longer show significantly large drought patterns in this area. In our analysis, no areas of drought are evident in Africa along the equatorial belt, as shown

in Figure 2, except for smaller areas (0N-0S, 20E) during 1988-2007. This could be related to the seasonal nature of the teleconnections (July-September, 3 months) being the determining factor.

In addition, no anticorrelation areas representative of droughts are detectable over India, Bangladesh and Myanmar. Northern Thailand is also almost uncovered, with a few exceptions during 2006-2019. Surprisingly, significant droughts occur almost consistently in the Andaman Sea region. Although this is also consistent with the teleconnection map in Figure 2, we would have suspected a seasonal character as in northern Thailand (February-June, 5 months).

In north Central China, which borders Mongolia, droughts occur during the El Niño phases described in Figure 2 during the months (June-October, 5 months). These are not observed in any of the 34 windows. Similarly, at the northwesternmost point of the United States, which forms the border with Canada, there are no droughts in the windows (November-March, 5 months). No window drought episodes were observed throughout the U.S. Territory.

The trend for the largest contiguous red area (Figure 3) in the Central Pacific shows a more stable trend than the largest blue area. As is known from the relevant literature, higher SST values in the Central Pacific are associated with more convection, as can be seen in Figure 2. As in Figure 2, the wall thickness of the largest correlating area in the western Central Pacific is also larger than in the eastern region in all windows. In addition to the extent of the largest correlating area along the equatorial belt in the Pacific, a branching in a southeasterly direction is observed, giving the largest red area similarity to a T-shape (ranges at times up to 10S-40S,120W-100W). Figure 2 does not show this similarity. The intersection begins in the 130W-150W region, and has a 45 degree southeast branch in addition to the equatorial extent. Although this does not always result in a continuous surface, Figure 5 (left) shows the possible dimensions of that branch. Furthermore, a westward shift is observed in a way that the Ecuadorian and Peruvian coasts are no longer touched, as can be seen from Figure 5 and is consistent with the observations from (Freund et al., 2019). In addition, a northerly arc around the Galapagos Islands can be noticed since 2006, as in Figure 5. The maximum extent of the largest correlating area is in the 1996 time window and is $9,402,819$ $km^2$, the minimum is in the last time window 2017 with $6,158,208$ $km^2$, while the average area from all time windows is $8,052,346$ $km^2$.

South America is known for its periods of flooding during El Niño phases, especially on the tropical west coast and in the southeastern part of the continent. (Cai et al., 2020). The southwestern area of South America around Chile (June-September, 4 months), shown in Figure 2, is visible only during the 1979-1990 period. Along the border between Brazil, Uruguay, Paraguay and Argentina, precipitation phases related to El Niño occur, especially from September to January (5 months), see Figure 2. Our study confirms the positive correlating influence of ONI for this region in the 1989-2020 time period. The east coast of Argentina, on the other hand, can be associated with El Niño exclusively in the 1993 and 1994 windows. Potential flooding over Bolivia and northern Paraguay, as seen in Figure 2 (April-October, 7 months), is not detected in any of the windows.

East Africa is affected by higher precipitation levels under El Niño conditions (September-January, 5 months), as shown in Figure 2. The region includes Somalia, Ethiopia, Kenya, and Tanzania and is confirmed in our analysis for the period 1988-2007. However, in the periods 1979-1987 and since 2008 (with the exception of the 2006 time window), hardly any signal is measurable, except in small areas over Somalia.

Figure 2 indicates high rainfall associated with El Niño in the southernmost part of India and Sri Lanka, especially during October-December (3 months). Influences were detected in our study exclusively in the 1998-2011 time range slightly further south (0N-5N,110E-120E). Figure 2 also

11

shows precipitation patterns in China, South Korea, and Japan (November-February, 4 months). The correlation windows show red teleconnections during 1989-2005, which are restricted to China (20N-30N,110E-120E).

In Central Asia, El Niño episodes are associated with increased precipitation, especially during January-April (4 months), see Figure 2. We can detect them in the correlation analysis in the time windows 1988-1991, 1994-2008, as well as 2011-2015. Interestingly, we can observe signals in both the northern part of the Arabian Peninsula and Iraq that are representative of precipitation during 1994-2017 and are not recorded as rainfall teleconnections in Figure 2.

The precipitation teleconnections in North America shown in Figure 2 are present primarily in the southern part of the United States, but also extend to northern Mexico. Our analysis can confirm this for the northern area of Baja California, the southwestern border with Mexico, for the 1993-2003 time windows. In this region, an influence is attributed in Figure 2 especially during the months of January-April (4 months). At times (1989-2001), the Gulf of California is also affected by El Niño-related precipitation, as are the regions around Phoenix and Las Vegas. In the 2002-2019 time frame, the influence appears to be confined around the southernmost tip of Baja California. In the southeastern part of the U.S. and in areas on the East Coast up to 40N, precipitation associated with high ONI values is observed in our studies during the period 1992-2018 (with the exception of the 2004 time window). According to Figure 2, flooding is associated with El Niño in this region for November-April (6 months). This could be one of the reasons why the signals in this region are observed for longer periods than in the southwestern regions of the country. Meanwhile, large, mostly red regions are observed in both the Atlantic and Indian Oceans. For the Atlantic Ocean, this is true for the 1984-1988 and 1996-2002 time windows. In the Indian Ocean, it is the 1996-1997 and 2013-2017 time windows. In Figure 2, such influences are unknown. Overall, we can identify 3 window-independent stable regions. These include the tropical Pacific, which is always positively correlated with ONI. The largest anticorrelating region is the Maritime Continent & the Southwest Pacific, which extends to 90W during its greatest extent in the first window in 1984. Other stable anticorrelating regions are found in South America, namely in the northern part of Brazil (Amazon region) and in the Darién Gap.
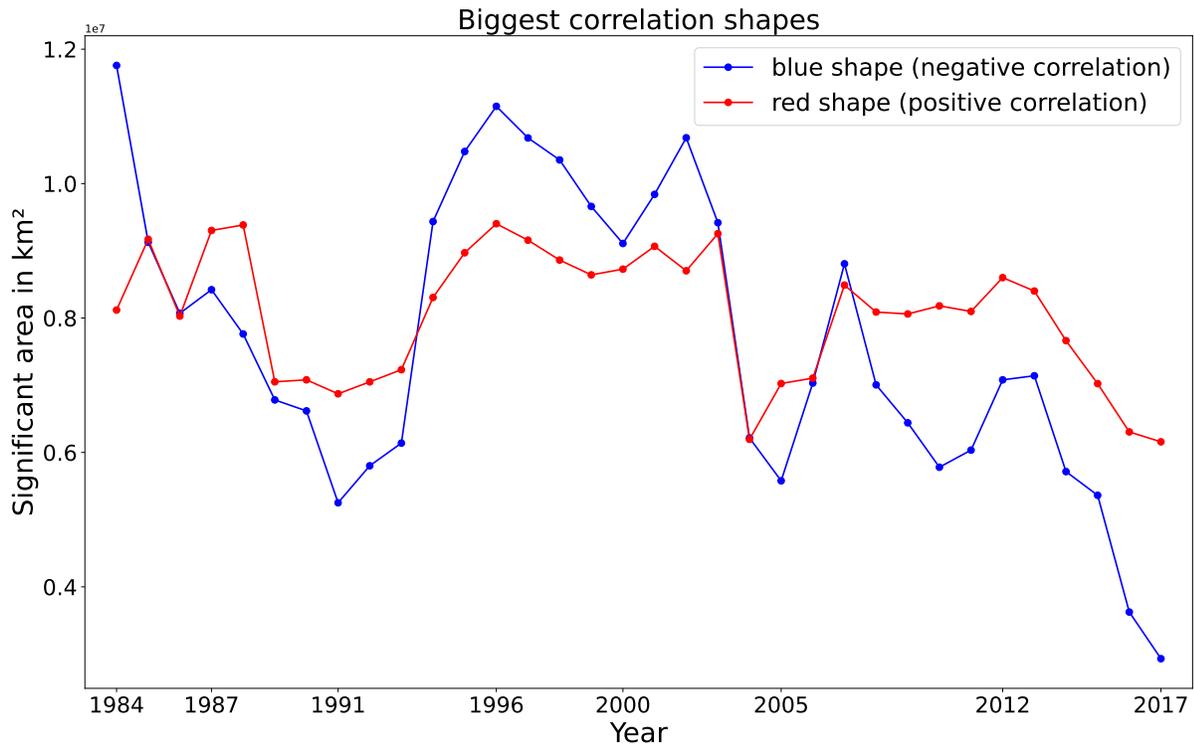
Fig 3: The Maritime Continent region & the southwestern Pacific region (blue) and Central Pacific Region (red) at significance level of $\alpha = 0.05$ after correcting for multiple comparisons with Benjamini-Hochberg method.
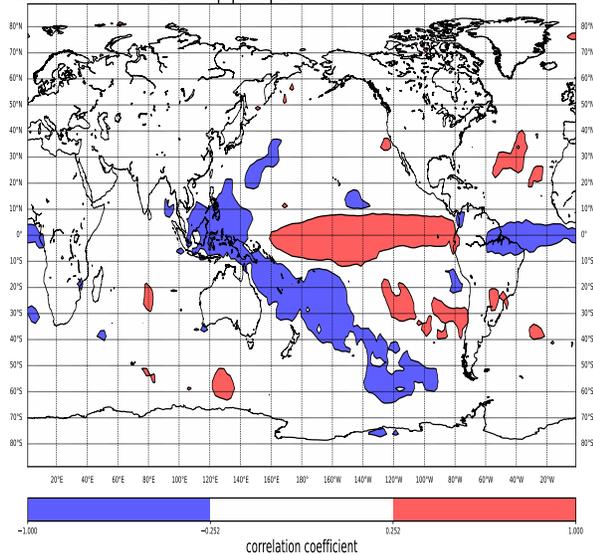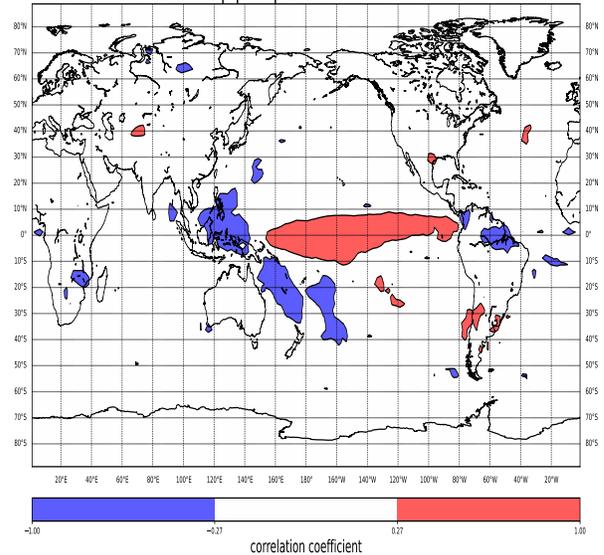


Fig 4: Correlation coefficient contours between Oceanic Niño Index and global precipitation anomalies for a 5% significance level with a false discovery rate correction. The analyzed time frames are 1979-1988 & 1986-1995 (120 months).
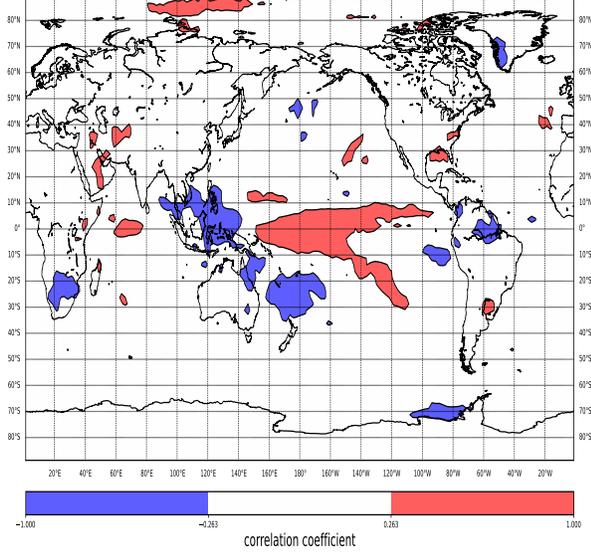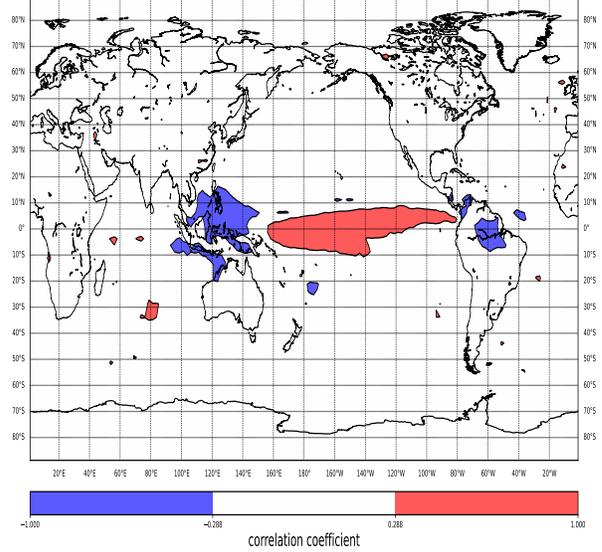
Fig 5: Correlation coefficient contours between Oceanic Niño Index and global precipitation anomalies for a 5% significance level with a false discovery rate correction. The analyzed time frames are 2000-2009 (120 months) & 2012-2021 (111 months).

### 4.1.2 Correlation Analysis Part 2

Next, we examine how the different ENSO indices (Nino 1+2, 3, 4, ONI) affect precipitation over different monthly lead times ($\tau_{min} = -1, \tau_{max} = -12$). Only interquartile ranges of IQR $<= 4$ are considered in the plots of medians for the respective grid points. Since the 10-year time windows start with $[1982, 1991]$ and end with $[2012, 2021]$, a total of 31 windows must be considered for each point. To seperate high peaks of the cross-correlation functions from noise, the dominant lags must be at least two standard deviations away from the mean of all Fisher z-transformations in the respective window. If this is not the case, no dominant lag is marked for the respective window at the corresponding location. In this analysis, only the absolute correlation values are considered, without distinguishing between droughts and above-average precipitation. Only grid points are shown where at least 12 of the 31 time windows have a dominant lag that meets the above conditions.

**Oceanic Niño Index**
Figures 6 shows the regions where the ONI is running ahead in time. In both subfigures, the teleconnections are immediately apparent, namely the two largest shapes (Pacific along the equatorial belt and Maritime Continent region + Southwest Pacific region, see Figure 2) from 4.1.1. In both subfigures, lag 1 ($\tau = -1$) dominates both the Maritime Continent and the Southwest Pacific Region. Interestingly, the region (west of Java Island, Indonesia) (5S-15S, 90E-110E) in Figure 6 (modes) shows increased lags in the range of 8-12. In contrast, the same region in Figure 6 (medians) is not affected by lags far in the past. In the Central Pacific along the equatorial belt, the north side of the belt from about 125W westward is largely dominated by lags 1 in both subfigures. It should be noted that the Niño 3.4 region begins at this point and extends westward to 170W. From about 6S (south of the equator), lags 2-4 are observed almost exclusively in the Central Pacific. East of the Niño 3.4 region, the teleconnections disappear south of the equatorial belt in the Pacific

Ocean. These observations are consistent with Figure 2. On the other side of the belt, namely in the 0N-4N region (north of the equator), lags 2-4 are exclusively dominant except for one grid point in Figure 6 (left) and two grid points in Figure 6 (right).

The teleconnections in South America in both subfigures are almost identical. The regions around the Darién Gap, the Colombian coast, northern Brazil, Guyana, Suriname, eastern Venezuela, and the eastern Amazon are consistent with 4.1.1. and Figure 2. The Darién Gap as well as the Colombian coast are dominated exclusively by lags 1. Only in the area around northern Brazil are there some grid points that are in the range of 2-4 lags. The Brazilian area exclusively shows a lag of 1, while the other regions tend to show a lag of 2.

We can also detect signals from East Africa, in the region around the border between Somalia, Kenya and Ethiopia. In Figure 6 (left), lag 1 is exclusively dominant here, and except for two grid points where lag 3 and lag 12 are dominant, lag 1 is also dominant in Figure 6 (right). In addition, teleconnections with predominantly lag 1 are seen east of the East African coasts. These teleconnections are also shown for ONI in 4.1.1 up to the year 2007. Signals from other regions, such as North America, South Africa, the Arabian Peninsula or Central Asia, could not be determined for ONI in contrast to lag 0 from 4.1.1. Globally, lag 1 is by far the most dominant for ONI.

**Niño 1+2 Index**

The Niño 1+2 region is the easternmost of all ENSO areas. The teleconnections from Figure 7 and show parallels to Figures 6 (ONI), although they are two spatially different regions. The exception is the Southwest Pacific region, where both medians and modes (Figure 7) are virtually unaffected by any dominant lags.

In the region west of Java Island, as in the case of ONI (Figure 6), dominant lags 10-12 are evident for both medians and modes. Along the equatorial belt in the Central Pacific, lags 2-5 tend to dominate, especially in the 160W-120W longitude range. North of the belt, lag 1 is most pronounced. Interestingly, along the belt (latitude 0), more and more lags in the 2-5 range are present as one approaches the Niño 1+2 region (0-10S, 90W-80W), especially lag 5 , as can be seen from Figure 7 (left). The teleconnections of South America from both subfigures almost match those of ONI, while East Africa has significantly fewer connections. Globally, the Niño 1+2 region is dominated by lag 1. As with the lag teleconnections in the ONI case, North America, South Africa, the Arabian Peninsula, and Central Asia lack any trace of the Niño 1+2 index in comparison to Figure 2.

**Niño 3 Index**

A look at Figure 8 shows that the regions affected by the Niño 3 index are almost identical to the ONI and are just as detectable in Figure 2. These include the Pacific Ocean along the Equatorial belt, the Maritime Continent + Southwest Pacific region, the Darién Gap, the Colombian coast, northern Brazil and Argentina, Guyana, Suriname, eastern Venezuela, the eastern Amazon and the border region between Somalia, Kenya and Ethiopia. This is consistent with the fact that the Niño 3 region covers a large portion (150W-120W) of the Niño 3.4 region associated with the ONI. No significant differences are discernible between both subfigures (modes and medians). Compared to Figure 6 both the plots of modes and medians west and north of Java Island have dominant lags in the range 8-12. It is also interesting to note that the regions around the Rio Parana (Argentina) and the region where the Amazon River crosses the Atlantic Ocean lead show a pronounced lag 3.

Particularly noteworthy is the fact that many lag 12 teleconnections are observed to the right of the Australian east coast. In addition, in contrast to Figure 6, signals are recorded over Iraq (mostly lag 1) and on the west coast of the United States (lags 2-5). The affected regions in East Africa show significantly more teleconnections than in the ONI case and extend into the Indian Ocean. Besides the region west and north of Java island, most teleconnections farther back than lag 1 are found south below the belt in the Central Pacific. Central America, most of Asia, and South Africa remain unaffected by the Niño 3 index. Globally, lag 1 is the most prevalent.

**Niño 4 Index**

Figure 9 shows the modes and medians of the Niño 4 index. The ENSO-affected regions in Figure 2 are only partially covered by the Niño 4 index. Interestingly, there is less overlap with ONI compared to the Niño 3 region, although part of the Niño 4 region (170W-150W) covers the ONI region (Niño 3.4). Furthermore, no lags are detectable in period 3-12, except for one grid point in Figure 9 (right) west of Java Island. The two largest regions from 4.1.1 are still detectable, but much less pronounced than in the other indices. From 150W eastward along the Equatorial belt in the Central Pacific, the influences decrease completely southward, just where the easternmost boundary of the Niño 4 region lies. With the exception of South America and the two largest areas from 4.1.1, the Niño 4 index does not appear to have any teleconnections globally when running ahead in time. Compared to lag 2, which is sporadic, lag 1 dominates in the aforementioned regions.
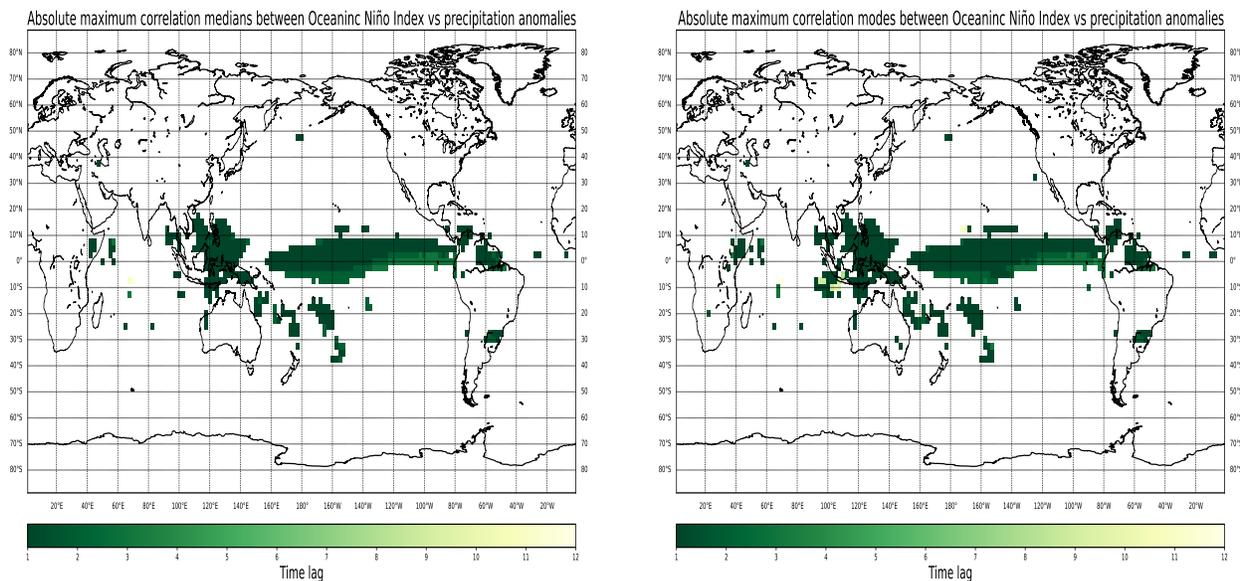


Fig 6: Left: Maximum absolute medians PCCs of ONI vs. PrecipAnom(lat,lon) from 31 (10-year) time windows for lags 1-12. None of the lags 5-10 are dominant. Right: Maximum absolute modes PCCs of ONI vs. PrecipAnom(lat,lon) from 31 (10-year) time windows for lags 1-12. None of the lags 5-7 are dominant.
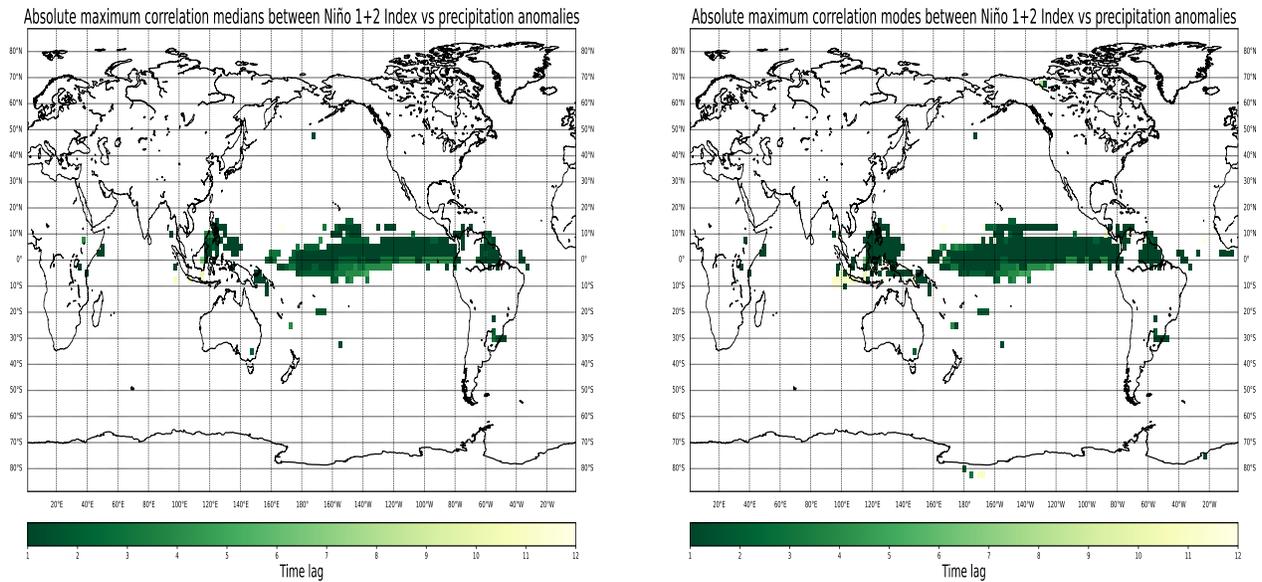
Fig 7: Left: Maximum absolute medians PCCs of Niño 1+2 vs. PrecipAnom(lat,lon) from 31 (10-year) time windows for lags 1-12. None of the lags 6 & 8-9 are dominant. Right: Maximum absolute modes PCCs of Niño 1+2 vs. PrecipAnom(lat,lon) from 31 (10-year) time windows for lags 1-12. None of the lags 6 & 9 are dominant.
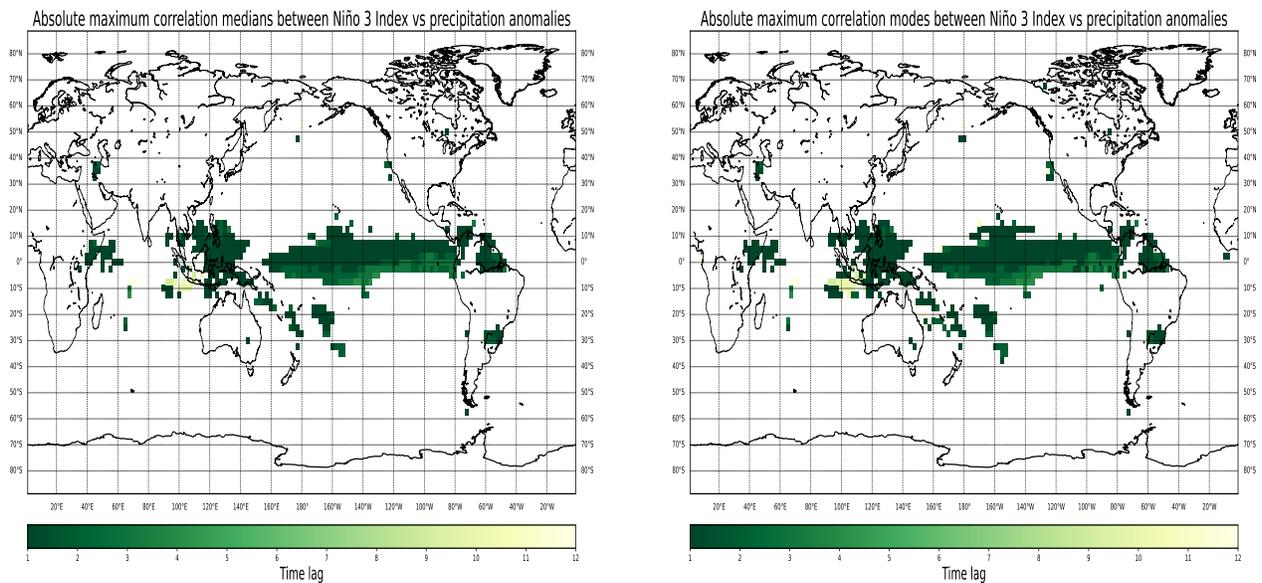


Fig 8: Left: Maximum absolute modes PCCs of Niño 3 vs. PrecipAnom(lat,lon) from 31 (10-year) time windows for lags 1-12. None of the lags 6-7 are dominant. Right: Maximum absolute modes PCCs of Niño 1+2 vs. PrecipAnom(lat,lon) from 31 (10-year) time windows for lags 1-12. None of the lags 6 & 9 are dominant.

17
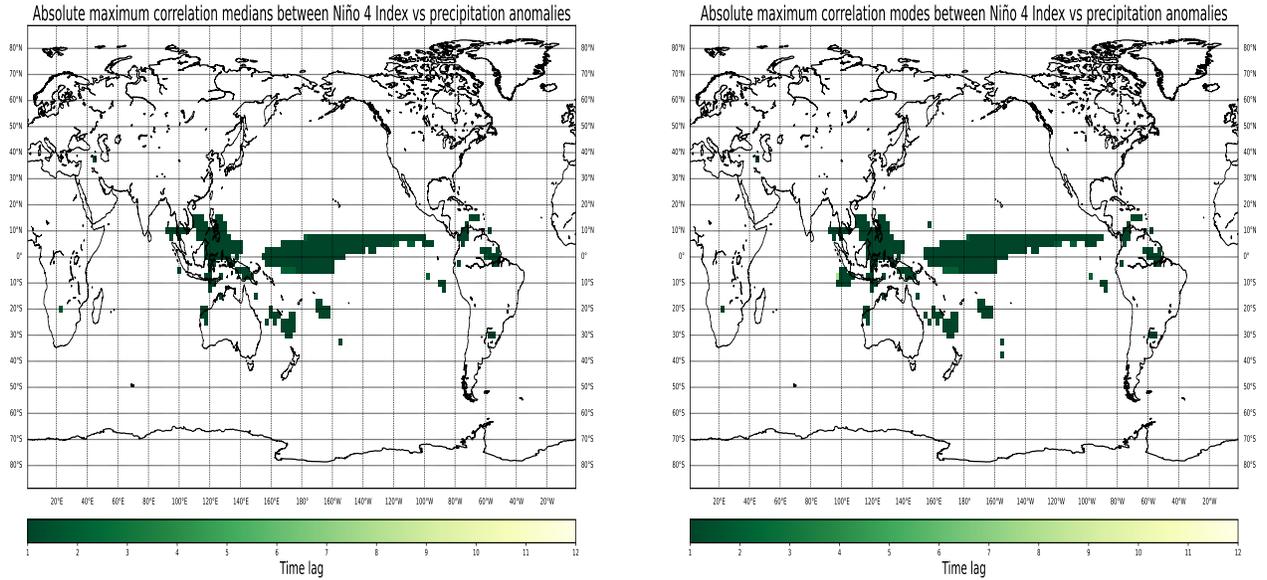
Fig 9: Left: Maximum absolute medians PCCs of Niño 4 vs. PrecipAnom(lat,lon) from 31 (10-year) time windows for lags 1-12. None of the lags 3-12 are dominant Right: Maximum absolute modes PCCs of Niño 4 vs. PrecipAnom(lat,lon) from 31 (10-year) time windows for lags 1-12. None of the lags 3-7 & 9-12 are dominant.

## 4.2 PCMCI without conditioning

In the following, we look at various Niño indexes using the PCMCI+CEN approach. In this section, we focus on not conditioning away other indices when considering a particular index. For PCMCI without conditioning, we only control for each index's own past history and the past precipitation anomalies of each grid point $F(lat, lon)$ ($\tau_{min} \in \{-1, 0\}$, $\tau_{max} = -12$, months). As described in 3.2, we consider instantaneous relationships that, strictly speaking, cannot be interpreted as causal processes. Nevertheless, we assume that ENSO is responsible for the anomalies in precipitation. As a complement to instantaneous relationships, we consider representations of beta coefficients that have $\tau_{min} = -1$ (without instantaneous links). These plots can be interpreted causally in terms of PCMCI without reservation. In addition to the 1982-2021 period, we also consider the 1982-2001 and 2002-2021 periods to draw possible conclusions about the evolution of the anomalies.

**Oceanic Niño Index**
Figure 10 (left) shows the causal map of ONI with instantaneous links. The largest positive correlating area is seen in the can be seen in the Central Pacific, but this only extends to about 120W compared to Figure 2. Interestingly, the easternmost boundary of the Niño 3.4 region is located right here. To our great surprise, we find many red areas in the equatorial region of the Maritime Continent, which are assigned to the largest anticorrelating region in both Figure 2 and the correlation analysis. In particular, in the area around Papa New Guinea, we find beta coefficients in the range $\beta \sim$ 1-5. If we omit the instantaneous links (Figure 10, right), they disappear almost completely. Red areas (positive precipitation anomalies) can also be seen along the equator in Indonesia, although not as strongly. Otherwise, blue dots predominate north of the equator (Maritime Continent) and in the Southwest Pacific region (Figure 11, left) and resemble the trend from the windows of the correlation analysis (negative $\beta \sim$ 0.2-0.6). Surprisingly, many blue areas of

18

influence ($\beta <=$-0.4) are also found in the region (20S-40S, 120W-80W), in a region where the correlation analysis finds positive correlations.

Droughts are predicted for northern Brazil (Figure 10 and 11) in the easternmost part of the Amazon River. This is as consistent with Figure 2 as it is with the correlation analysis. Also, many regions of the U.S. that are associated with increased precipitation in the El Niño case (Figure 2) can be confirmed in Figure 10 and 11. Surprisingly, positive beta values $\beta \sim$ 0.2-0.4 are over Puerto Rico, as well as in Arctic Russia (85N, 100E-120E). Also worth mentioning are anticorrelating teleconnections in far eastern Russia (80N-60N,140E-160E), which are in the range of negative $\beta \sim$ 0.1-0.4, and can be detected exclusively in the 1985 and 1986 windows.

East Africa shows positive as well as negative clusters of teleconnections, while the red areas disappear completely without the instantaneous links. We suspect that the red ones are seasonal (September-January, 5 months), while the blue ones tend to the southern part of the continent (see Figure 2). eastern Turkey is one of the few regions in the world that has several dominant lags that run relatively far ahead in time (lag 7). Otherwise, instantaneous links (lag 0) dominate the causal maps in Figure 10 (left) and lag 1 in Figure 10 (right). Interestingly, Figures 6 (left and right) are much more similar to the instantaneous links from Figures 10 (left), 11 (left), and 24 (right) than from Figure 10 (right), which could be related to the fact that ENSO indices are generally highly autocorrelated (Sajani Surendran et. al., 2015).

Omitting the instantaneous links, Figure 10 (right) shows that the positive precipitation anomalies in the Central Pacific disappear completely. Large areas of the largest anticorrelating surfaces on the Maritime Continent also disappear. The remaining regions of the world are almost identical to Figure 10 (with the exception of (20S-40S, 120W-80W), indicating that ONI influences are felt at least a month later in these regions.

Figure 12 (left and right) shows the instantaneous links for the 1982-2001 and 2002-2021 periods, respectively. In Figure 24 (left), the largest blue anticorrelating region and the largest red correlating region are both largely preserved. Figure 24 (left) also shows negative beta coefficients in the range of $\beta \sim$ 0.4-0.8 in the region southwest of South America, as already shown for the 1998-2007 period in 4.1.1. Also of interest are positive beta values in the range of $\beta \sim$ 0.4-0.8 in eastern Turkey on the doorstep of the Arabian Peninsula.

Figure 24 (right) shows approximately the T-branch of the correlation analysis in the Central Pacific. The regions around northern Brazil, Guyana, Suriname, eastern Venezuela, and the eastern Amazon are consistent with 4.1.1. and Figure 2 and are clearly identifiable over the 2002-2021 period with beta values in the negative range up to $\beta \sim$ 1-5. A negative range (see Figure 24, right) is also evident in the northern Pacific ($\beta \sim$ 1-5), as can also be seen in Figure 2.

Not much can be said about the evolution of the teleconnections, since in some cases regions appear that were not seen before. The only stable red region is the tropical Pacific, while a weakening is observed on the anticorrelating Maritime Continent & Southwest Pacific Region. We have already seen this finding in Figure 3 of the correlation analysis.
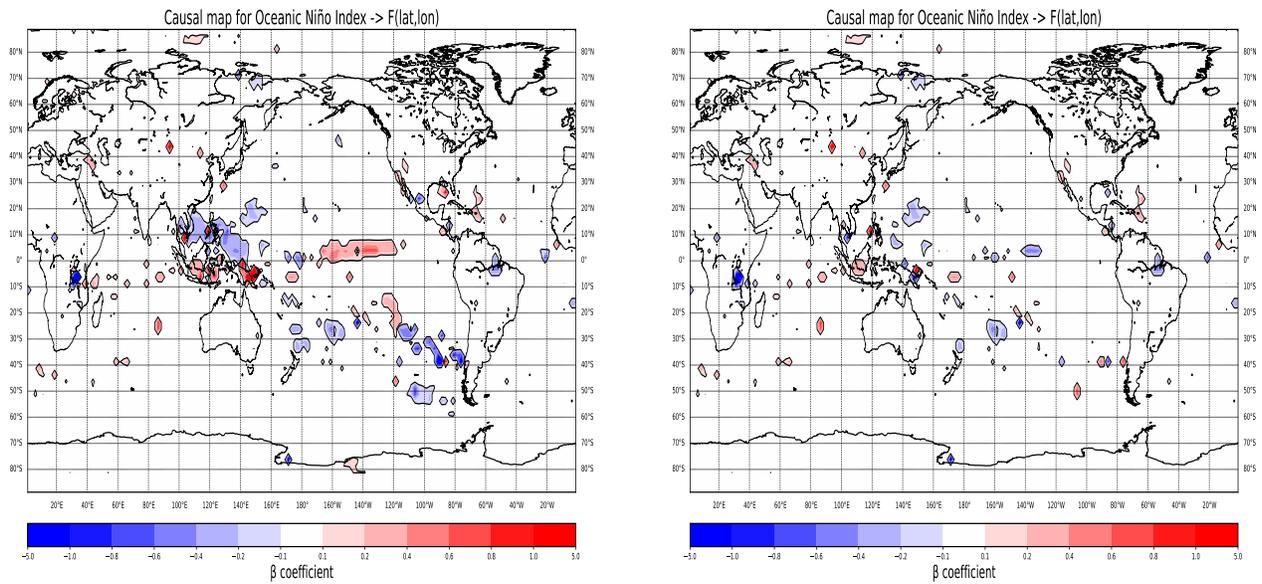
Fig 10: Left: Maximum absolute $\beta$ coefficients for the link ONI $\rightarrow$ PrecipAnom(lat,lon) for lags 0-12 (ONI runs ahead in time plus instantaneous links) obtained from PCMCI followed by standardized multiple linear regression. The trained time period is 1982-2021 (471 months). Right: Without instantaneous links.
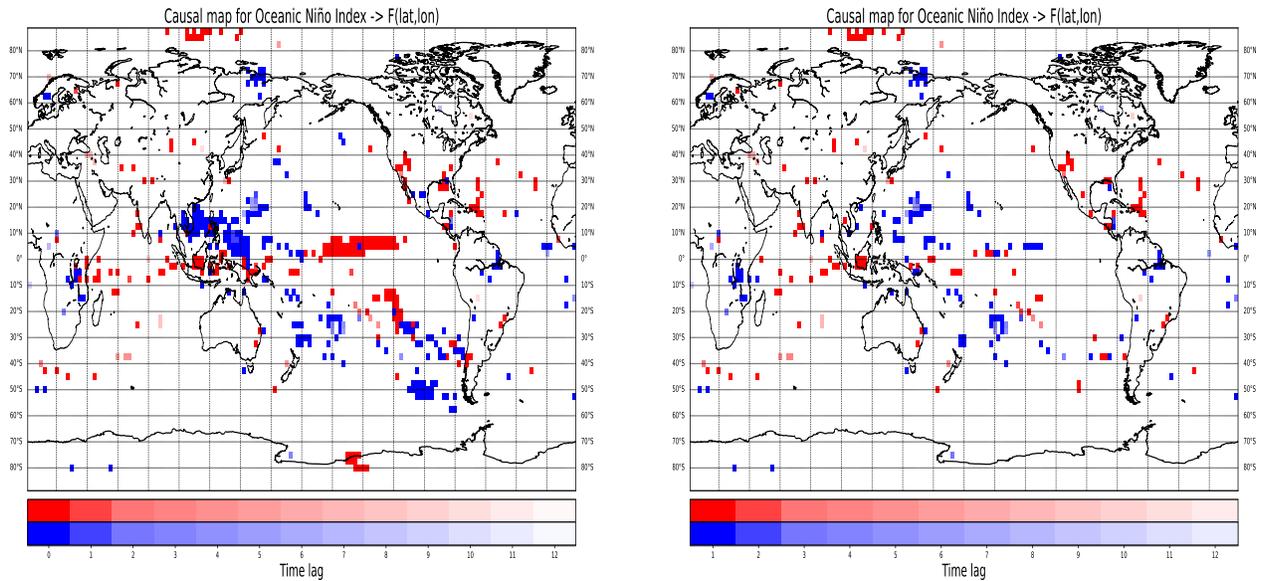


Fig 11: Left: Dominant time lags for the link ONI $\rightarrow$ PrecipAnom(lat,lon) for lags 0-10 (ONI runs ahead in time plus instantaneous links) obtained from PCMCI followed by standardized multiple linear regression. The trained time period is 1982-2021 (471 months). None of the lags 11-12 are dominant. Red dots represent $\beta_j >= 0.1$, blue dots represent $\beta_j <= -0.1$. Right: Without instantaneous links. None of the lags 11-12 are dominant.
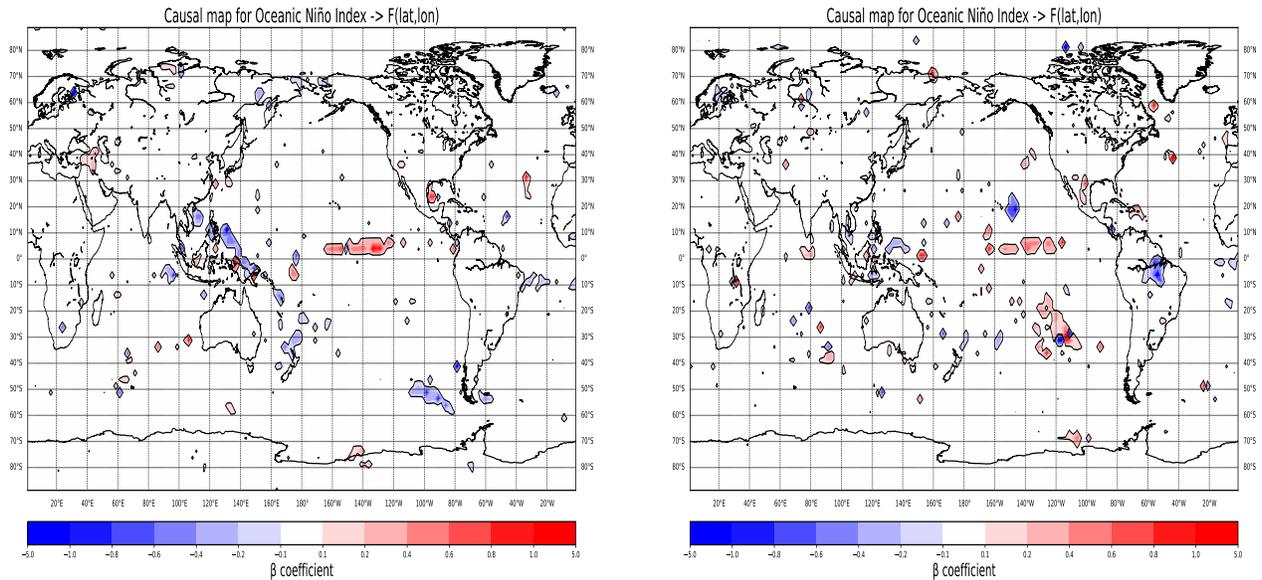
Fig 12: Left: Maximum absolute $\beta$ coefficients for the link ONI $\rightarrow$ PrecipAnom(lat,lon) for lags 0-9 (ONI runs ahead in time plus instantaneous links) obtained from PCMCI followed by standardized multiple linear regression. The trained time period is 1982-2001 (240 months). None of the lags 10-12 are dominant. Right: Maximum absolute $\beta$ coefficients for the link ONI $\rightarrow$ PrecipAnom(lat,lon) for lags 0-9 (ONI runs ahead in time plus instantaneous links) obtained from PCMCI followed by standardized multiple linear regression. The trained time period is 2002-2021 (231 months). None of the lags 10-12 are dominant.

### Niño 1+2 Index

Figure 13 shows the influences of Niño 1+2 on global precipitation anomalies during 1982-2021. Interestingly, the PCMCI+CEN algorithm for Figure 13 (left) shows negative precipitation ($\beta \sim$ 0.4-5) anomalies starting at 150W eastward in the Central Pacific, which are absolutely unexpected. These largely disappear (except in the area below the equatorial belt 110W-95W) when the instantaneous links are dropped, see Figure 13 (right). Figure 13 (right) is more consistent with expectations for the Central Pacific, not least because the red correlated region (positive precipitation anomalies) extends into the Niño 1+2 region. Omitting the instantaneous connections often reverses the signs of the beta coefficients.

Just offshore in eastern South America (10S-20S), ENSO-associated droughts (negative $\beta \sim$ 0.4-0.6) also occur, as shown in Figure 2 (September-December, 4 months). These transform into positive precipitation anomalies in the range ($\beta \sim$ 0.4-1) when $\tau_{min} = -1$ is considered, as shown in Figure 13 (right) and Figure 26 (right). Also, large blue regions (negative $\beta \sim$ 0.2-0.8) can be seen west of the South American coast (west of Chile). Compared to the PCMCI without conditioning in the ONI case, the Darién Gap as well as the northern coast of Colombia are surrounded by blue teleconnections (as seen in Figure 2) that are negative in the range $\beta \sim$ 0.2-0.8 for the Niño 1+2 index. It is interesting to observe the soup of red and blue teleconnection fields in the 110W-75W, 50S-70S region ($\beta \sim$ 0.2-0.8) in Figure 13 (left), which turn red without instantaneous connections, see Figure 13 (right). From the correlation analysis for ONI, it appears that these regions are frequently associated with droughts (blue), while they are not evident in Figure 2.

The Maritime Continent, on the other hand, shows both red and blue dots and areas (Figure 13), but is nowhere near as clearly visible as in ONI. Especially in the equatorial region, unexpected

positive precipitation anomalies are again visible ($\beta \sim 0.4$-$0.6$). In particular, west of Java Island, both blue and red dots are visible for lag 0 (see Figure 14, left) and lag 1 (see Figure 14, right), here exclusively positive precipitation anomalies), indicating that the effects of the Niño 1+2 index occur at least one month later. In comparison, the correlation analysis from 4.1.2 indicates dominant lags much further back in time in months, see Figure 7.

Also of interest are the effects of the positive precipitation anomalies ($\beta \sim 0.1$-$0.2$) east of the East African coast, west of the Indian coast, south of South Korea, and in some areas of Central Asia, consistent with Figure 2. The Caspian Sea area shows grid points with $\tau = -7$ (month) as the dominant lag, similar to the ONI case.

Looking at the 1982-2001 and 2002-2021 periods (Figure 15), we find that the Central Pacific near the equator loses the blue trace from 1982-2001 in the 2002-2021 period, as would be expected from Figure 2. It remains puzzling why the 1982-2001 period in particular predicts negative precipitation anomalies in the Central Pacific. Also of interest are positive precipitation anomalies in eastern Canada with beta coefficients $\beta \sim 0.2 - 0.8$ in Figure 27 (right). With the exception of the blue regions in the Central Pacific, north of the Surinam coast in South America and in far eastern Russia, there are no stable regions, so no valid conclusions can be drawn about the evolution of teleconnections for Niño 1+2.
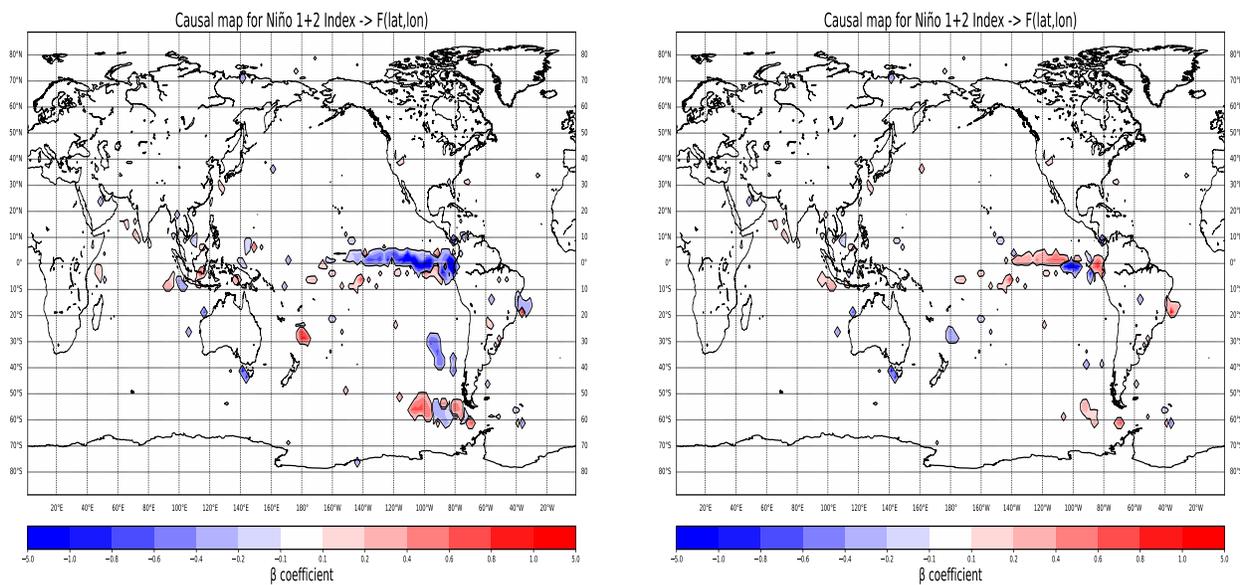


Fig 13: Left: Maximum absolute $\beta$ coefficients for the link Niño 1+2 → PrecipAnom(lat,lon) for lags 0-12 (Niño 1+2 runs ahead in time plus instantaneous links) obtained PCMCI followed by standardized multiple linear regression. The trained time period is 1982-2021 (471 months). Right: Without instantaneous links.
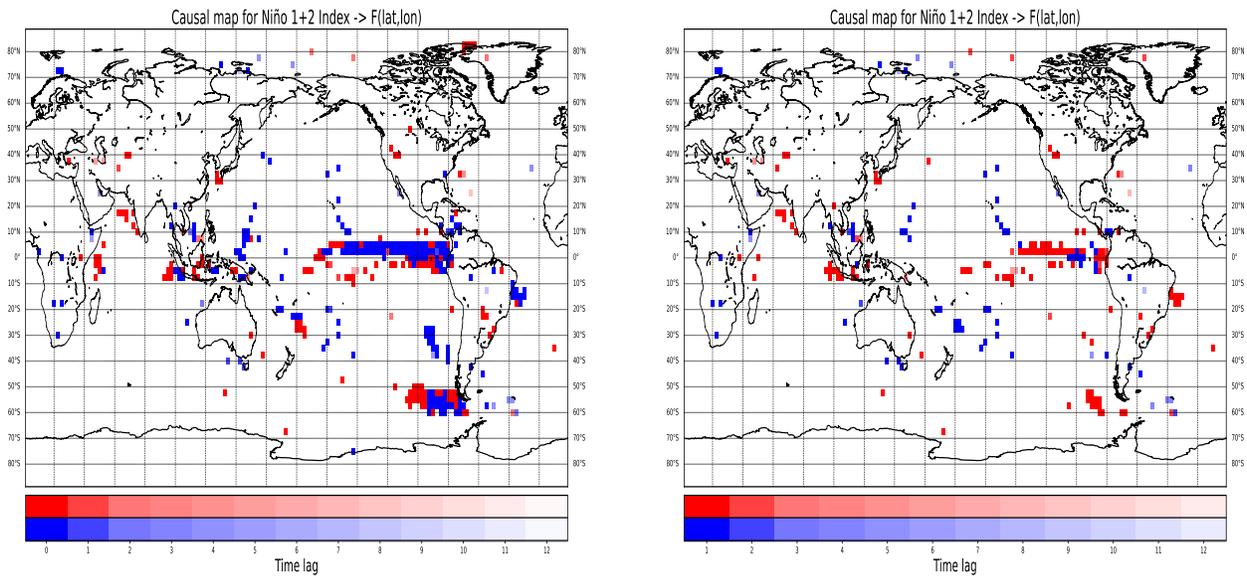
Fig 14: Left: Dominant time lags for the link for the link Niño 1+2 → PrecipAnom(lat,lon) for lags 0-10 (Niño 1+2 runs ahead in time) obtained from PCMCI followed by standardized multiple linear regression. The trained time period is 1982-2021 (471 months). None of the lags 11-12 are dominant. Red dots represent $\beta_j >= 0.1$, blue dots represent $\beta_j <= -0.1$. Right: Without instantaneous links.
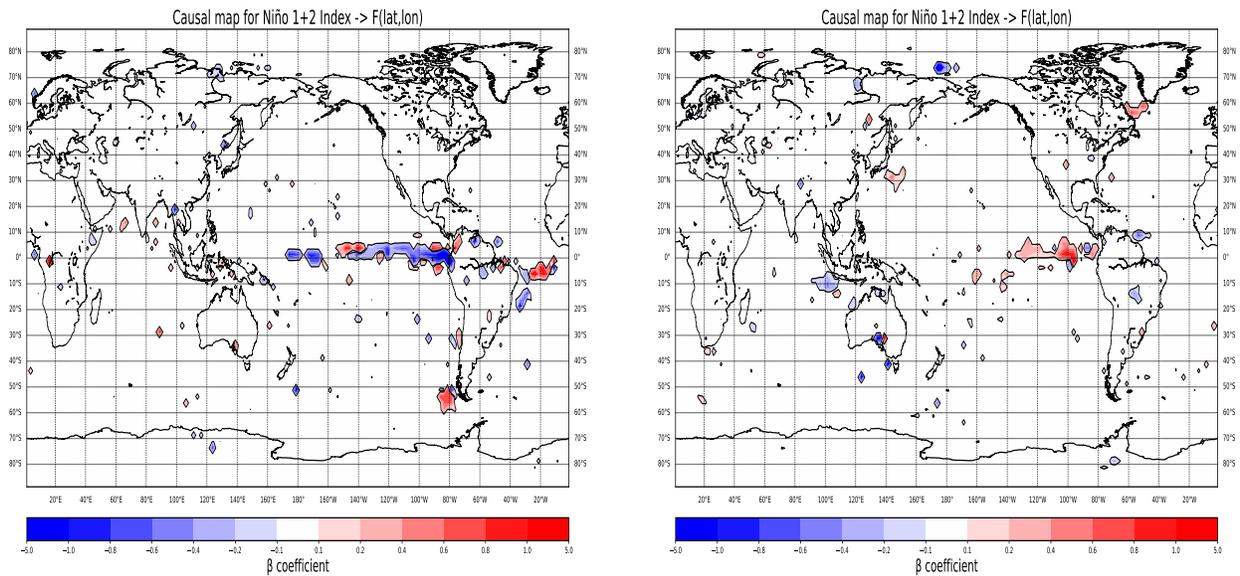


Fig 15: Left: Maximum absolute $\beta$ coefficients for the link Niño 1+2 → PrecipAnom(lat,lon) for lags 0-8 (Niño 1+2 runs ahead in time plus instantaneous links) obtained from PCMCI followed by standardized multiple linear regression. The trained time period is 1982-2001 (240 months). None of the lags 9-12 are dominant. Right: Maximum absolute $\beta$ coefficients for the link Niño 1+2 → PrecipAnom(lat,lon) for lags 0-10 (Niño 1+2 runs ahead in time plus instantaneous links) obtained from PCMCI followed by standardized multiple linear regression. The trained time period is 2002-2021 (231 months). None of the lags 11-12 are dominant.

23

**Niño 3 Index**

Next, we compute the causal maps without conditioning for the Niño 3 index. Figure 16 shows the beta values for both instantaneous links and $\tau_{min} = -1$. In many respects, the causal map for the 1982-2021 (Figure 16) period of Niño 3 resembles that of ONI. The largest red area is again found in the Central Pacific, unlike ONI's causal map (Figure 11, left), this one extends to the Equadorian and Peruvian coasts with many values in the $\beta \sim$ 0.2-0.4 range, but also some in the $\beta \sim$ 1-5 range. A trace of the T-shape mentioned from 4.1.1 is evident in the Central Pacific. Interestingly, negative beta coefficients in the range $\beta \sim$ 1-5 are found now and then, especially strong between 130W-110W. From about 170W westward the largest red area ceases, and blue teleconnections in the negative range $\beta \sim$ 0.2-0.6 are found in the range 170E-170W.

Consistent with Figure 2 for the 1982-2021 period are the regions of greatest correlating area in the Central Pacific, the Maritime Continent with majority blue teleconnections, Brazil south of the Amazon River (negative $\beta \sim$ 0.1-0.2), the U.S. ($\beta \sim$ 0.1-0.2), and a small area at the southernmost point of Japan with beta values $\beta \sim$ 0.1-0.2. The Maritime Continent has more red teleconnections representative of positive precipitation anomalies in the 130E-150E range compared to ONI's causal map, but also some over Java Island as well as along the equator.

Compared to Figure 8 from 4.1.2, the dominant lags from Figure 17 show greater spatial variability. Both east Africa and the Southwest Pacific are not affected by dominant Niño 3 lags in the correlation analysis. Interestingly, many red teleconnections disappear when the instantaneous links over the Maritime Continent and along and over the equatorial belt in the Pacific are omitted, as can be seen from Figure 16 (right). From 20S southward, blue teleconnections disappear without the instantaneous links, such as (negative $\beta \sim$ 0.2-0.8) west of the South American coast (west of Chile) or 110W-75W and 50S-70S region (negative $\beta \sim$ 0.2-0.8). In Figure 16 (instantaneous links), lag 0 dominates, while in Figure 16 (right), lag 1 dominates. Figure 18 shows the 1982-2001 and 2002-2021 periods, respectively. The most stable regions are located in the central Pacific around the equator and extend to about 180W, but no longer touch the South American coast in the 2002-2021 period. Moreover, the number of beta values decreases significantly in the range of $\beta \sim$ 1-5 values in Figure 18 (right). On the Maritime Continent, the blue teleconnections with beta coefficients (negative $\beta \sim$ 1-5) (during the 1982-2001 period) shift from north of Indonesia and the Phillipines toward near the equator, see Figure 18 (right), with the red teleconnections from Figure 18 (left) ($\beta \sim$ 1-5), which were unexpected in this region, almost completely disappearing. However, a decrease in blue teleconnections in the Maritime Continent is not evident.

Another observation is the blue teleconnections (negative $\beta \sim$ 0.1-0.8) in northern Canada for the 1982-2001 period and the red teleconnections in eastern Canada $\beta \sim$ 1-5 for the 2002-2021 period. During the 2002-2021 period, we make similar observations for the red teleconnections associated with Niño 1+2.
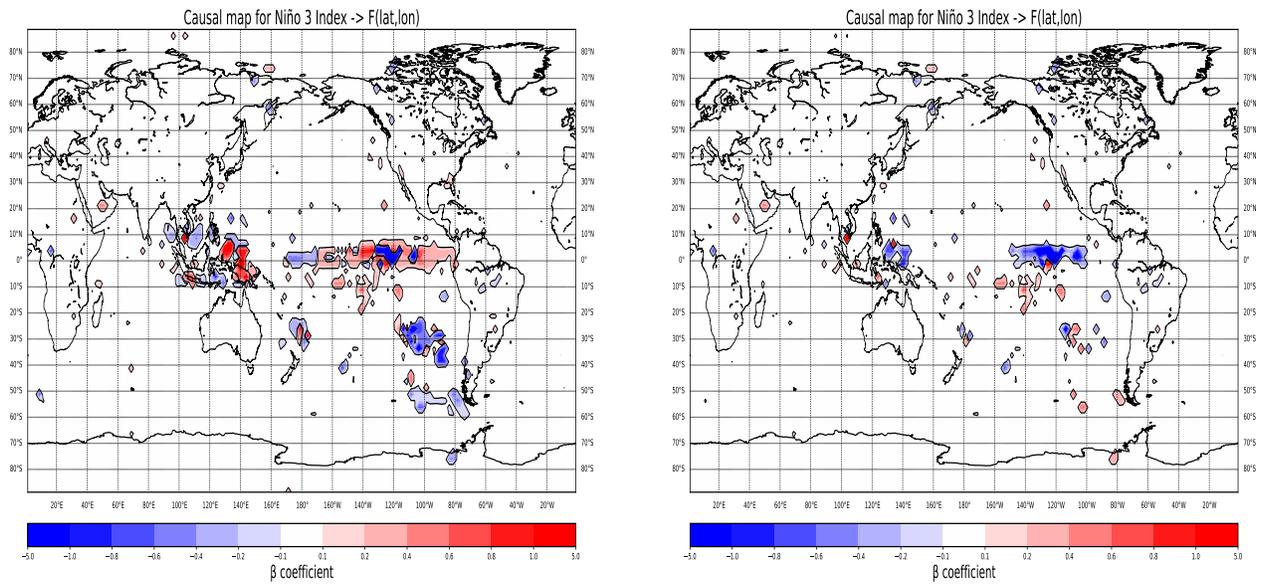
Fig 16: Left: Maximum absolute $\beta$ coefficients for the link Niño 3 $\rightarrow$ PrecipAnom(lat,lon) for lags 0-12 (Niño 3 runs ahead in time plus instantaneous links) obtained from PCMCI followed by standardized multiple linear regression. The trained time period is 1982-2021 (471 months). Right: Without instantaneous links.
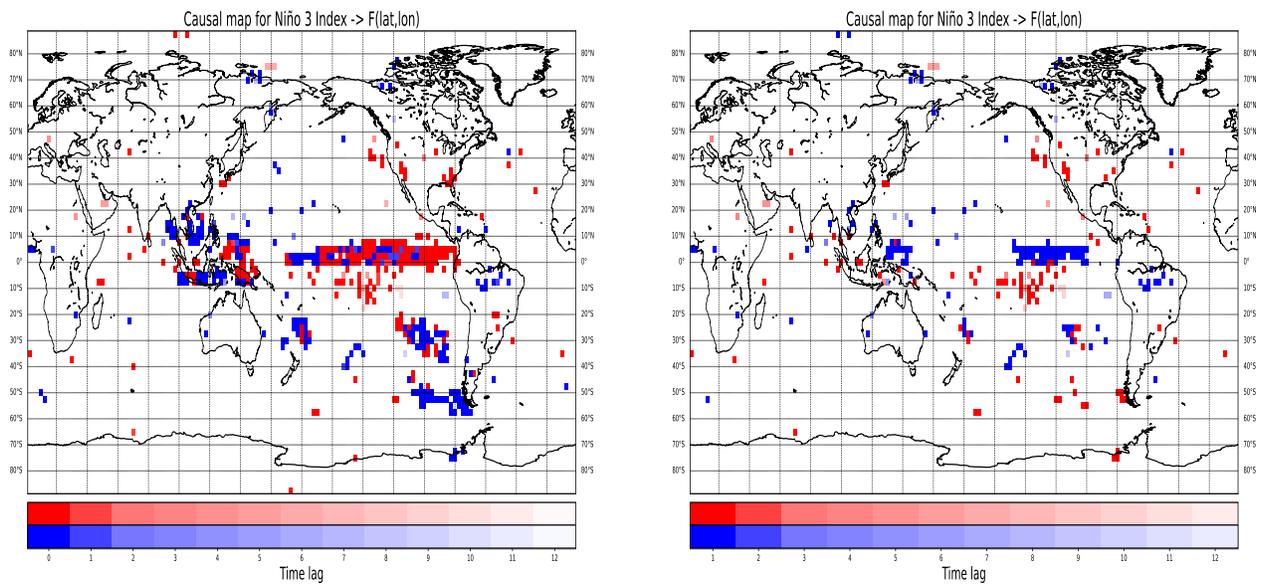


Fig 17: Left: Dominant time lags for the link Niño 3 $\rightarrow$ PrecipAnom(lat,lon) for lags 0-8 (Niño 3 runs ahead in time plus instantaneous links) obtained from PCMCI followed by standardized multiple linear regression. The trained time period is 1982-2021 (471 months). None of the lags 9-12 are dominant. Red dots represent $\beta_j >= 0.1$, blue dots represent $\beta_j <= -0.1$. Right: Without instantaneous links. None of the lags 9-12 are dominant.
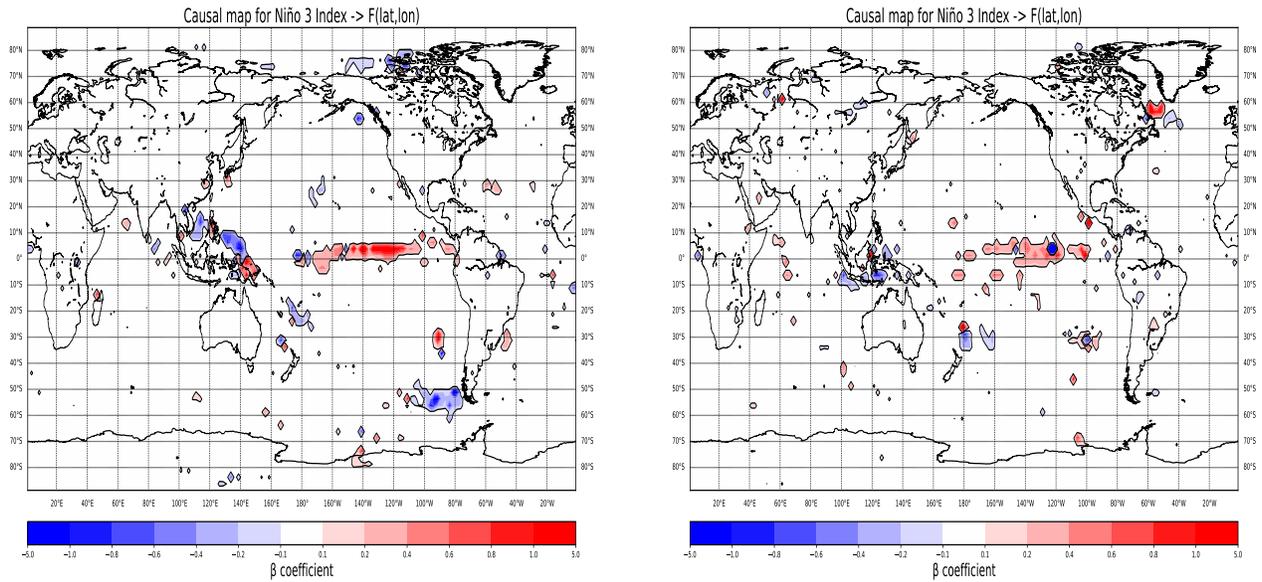
Fig 18: Left: Maximum absolute $\beta$ coefficients for the link Niño 3 $\rightarrow$ PrecipAnom(lat,lon) for lags 0-10 (Niño 3 runs ahead in time plus instantaneous links) obtained from PCMCI followed by standardized multiple linear regression. The trained time period is 1982-2001 (240 months). None of the lags 11-12 are dominant. Right: Maximum absolute $\beta$ coefficients for the link Niño 3 $\rightarrow$ PrecipAnom(lat,lon) for lags 0-9 (Niño 3 runs ahead in time plus instantaneous links) obtained from PCMCI followed by standardized multiple linear regression. The trained time period is 2002-2021 (231 months). None of the lags 10-12 are dominant.

**Niño 4 Index**

A look at Figure 19 shows the causal maps for Niño 4. Disregarding instantaneous links, large areas disappear over the Maritime Continent, the Southwest Pacific, and along the Central Pacific (170W-150W). In most other regions, the effects of the Niño 4 index are still felt at least a month later (at dominant lag 0), as can be seen from Figure 19 (right). Like the Niño 3 index, the Niño 4 index resembles the causal map of ONI from Figures 10 and 11, especially over the Maritime Continent & Southwest Pacific, South America, the Indian Ocean and the United States. Compared to the correlation analysis in Figure 9, PCMCI without conditioning exhibits significantly greater spatial variability.

Along the Central Pacific to 150W (north of the equatorial belt), the easternmost boundary of the Niño 4 region, positive precipitation anomalies end ($\beta \sim$ 0.2-0.8) until they reappear only in the region (110W-100W) above the equatorial belt ($\beta \sim$ 0.4-5). Along the Central Pacific to 150W (north of the equatorial belt), the easternmost boundary of the Niño 4 region, the positive precipitation anomalies end ($\beta \sim$ 0.2-0.8) until they reappear ($\beta \sim$ 0.4-5) only in the region (110W-110W) above the equatorial belt. Positive precipitation anomalies in the Central Pacific region are in harmony with Figure 2.

The Maritime Continent over the Philippines area (negative $\beta \sim$ 0.4-5) and the Southwest Pacific (negative $\beta \sim$ 0.4-5) have negative precipitation anomalies consistent with Figure 2. Not consistent with Figure 2 are again, as with Nino 1+2, 3, and ONI, positive precipitation anomalies around the southern equatorial region, particularly over western Indonesia (0S-10S, 100E-120E). In addition, we can detect other ENSO regions from Figure 20 consistent with Figure 2, namely blue teleconnections in Brazil (0S-10S, negative $\beta \sim$ 0.2-0.4), red teleconnections in Central Asia

26

($\beta \sim 0.6$-5) and Russia (not in Figure 2), and over the USA ($\beta \sim 0.4$-0.6).

Furthermore, some red teleconnections are found on the Black Sea coast over Turkey and Bulgaria ($\beta \sim 0.2$-0.4) and in Eastern Canada ($\beta \sim 1$-5). Both the Indian Ocean and North Atlantic have many positive precipitation anomalies, the cause of which often lies further in the past (dominant lags 2-9). In contrast, blue teleconnections dominate in the North and South Pacific. Globally, lag 0 is dominant in Figure 20 (left) and lag 1 in Figure 20 (right).

Figure 21 shows the time periods 1982-2001 and 2002-2021 of the causal maps for the Niño 4 region. For the largest correlating area in the Central Pacific, an eastward shift can be seen crossing the easternmost Niño 4 boundary. In addition, a trace of the T-shape from 4.1.1 can be seen in Figure 27 (right). The Maritime Continent shows significantly fewer blue teleconnections during 2002-2021 compared to 1982-2001. This could be related to the observation from Figure 3. In contrast, the Southwest Pacific region appears to be relatively stable, as are some regions in the Central Atlantic and Indian Ocean. The increase in red teleconnections in Central Asia and Russia is interesting, while there are some teleconnections in the $\beta \sim 1$-5 region. In the 2002-2021 period, some red teleconnections even extend to the Black Sea. More positive precipitation anomalies are also observed in North America during 2002-2021, especially south of the Baja California $\beta \sim$ 1-5, area (20N-10N, 85W-55W), but as with all other Niño indices for 2002-2021, strong positive precipitation anomalies are observed in eastern Canada $\beta \sim 0.6$-5. Red and blue teleconnections are particularly noticeable in the polar regions in both Figure 27 (left and right).
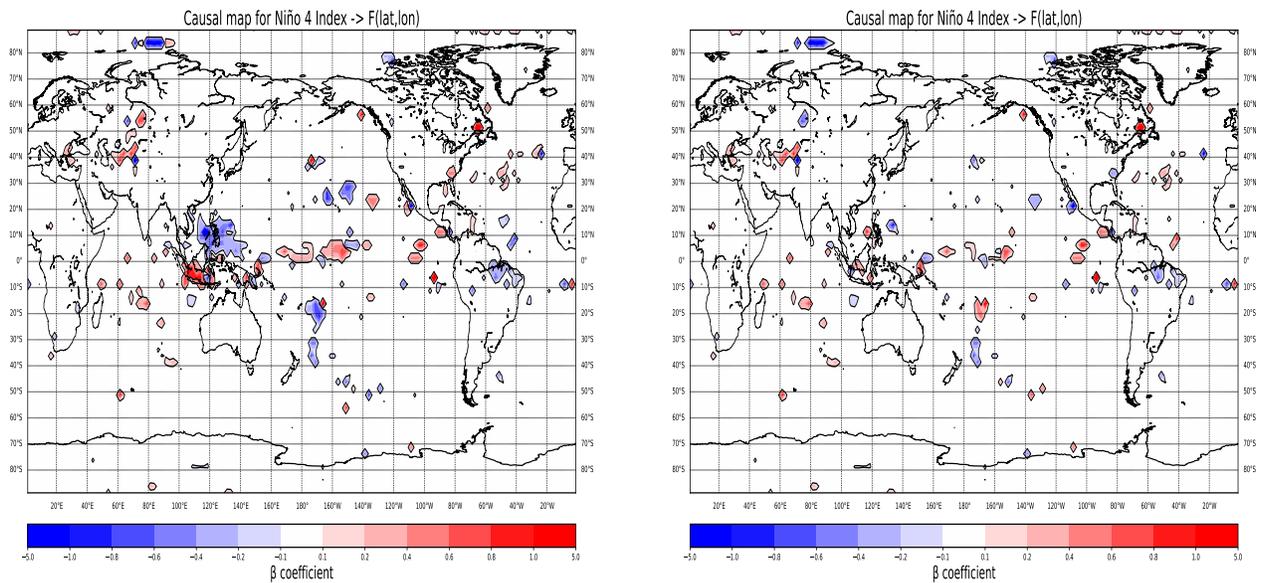


Fig 19: Left: Maximum absolute $\beta$ coefficients for the link Niño 4 $\rightarrow$ PrecipAnom(lat,lon) for lags 0-12 (Niño 4 runs ahead in time plus instantaneous links) obtained from PCMCI followed by standardized multiple linear regression. The trained time period is 1982-2021 (471 months). Right: Without instantaneous links.
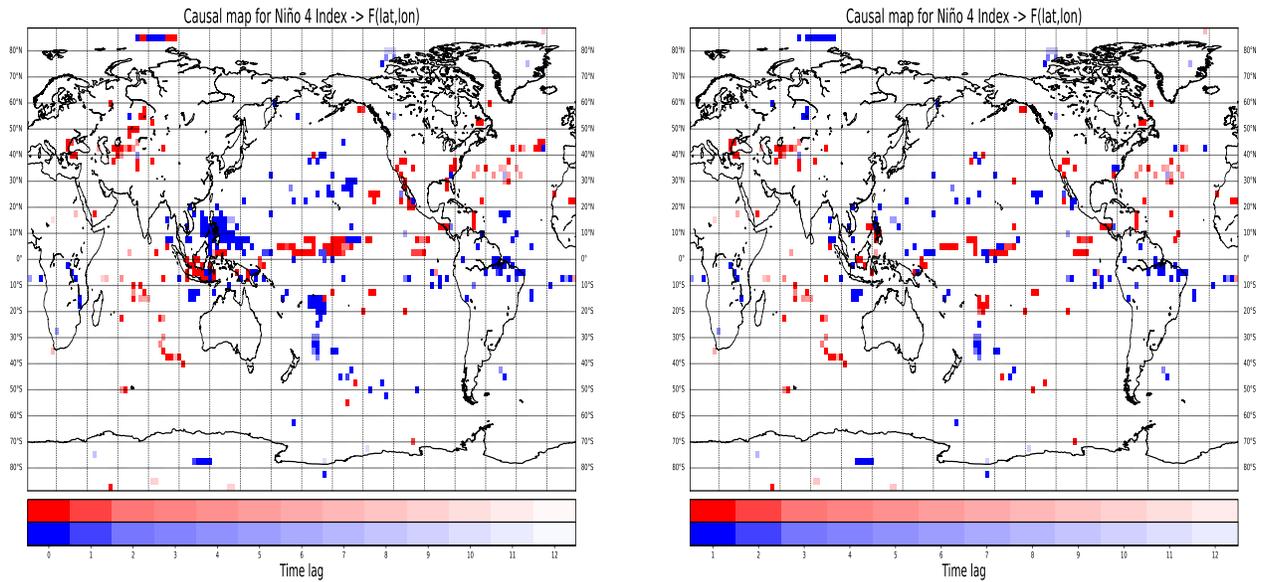
Fig 20: Left: Dominant time lags for the link Niño 4 → PrecipAnom(lat,lon) for lags 0-10 (Niño 4 runs ahead in time plus instantaneous links) obtained from PCMCI followed by standardized multiple linear regression. The trained time period is 1982-2021 (471 months). None of the lags 11-12 are dominant. Red dots represent $\beta_j >= 0.1$, blue dots represent $\beta_j <= -0.1$. Right: Without instantaneous links. None of the lags 11-12 are dominant.
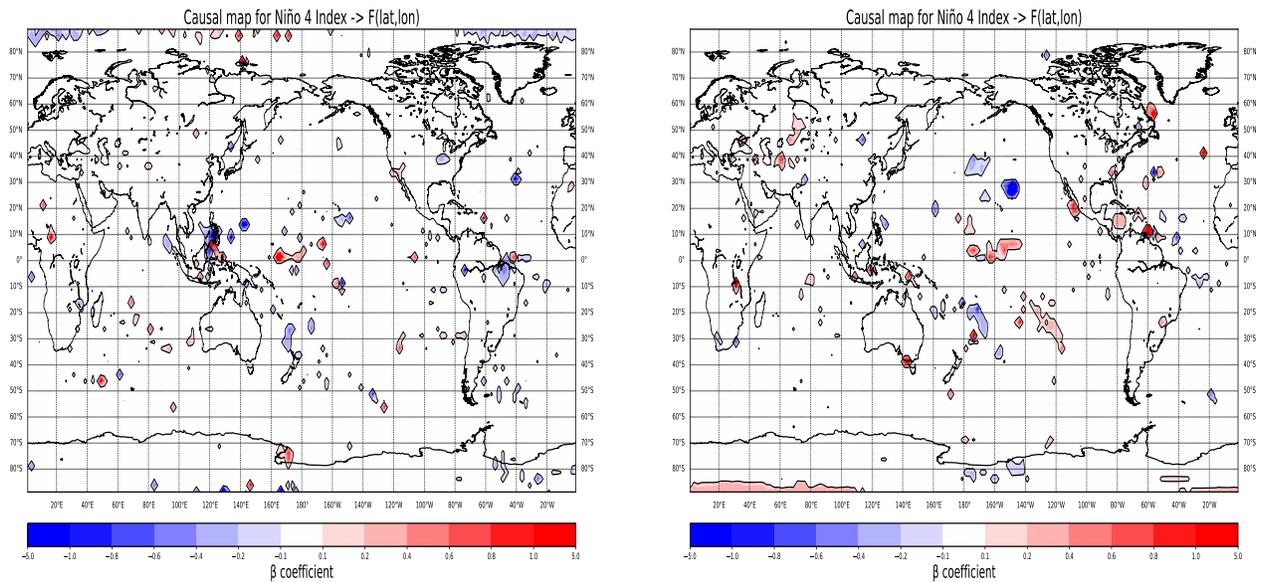


Fig 21: Left: Maximum absolute $\beta$ coefficients for the link Niño 4 → PrecipAnom(lat,lon) for lags 0-10 (Niño 4 runs ahead in time plus instantaneous links) obtained from PCMCI followed by standardized multiple linear regression. The trained time period is 1982-2001 (240 months). None of the lags 11-12 are dominant. Right: Maximum absolute $\beta$ coefficients for the link Niño 4 → PrecipAnom(lat,lon) for lags 0-10 (Niño 4 runs ahead in time plus instantaneous links) obtained from PCMCI followed by standardized multiple linear regression. The trained time period is 2002-2021 (231 months). None of the lags 11-12 are dominant.

28

### *4.3 PCMCI with conditioning*

Finally, we examine the causal maps of PCMCI+CEN by removing the influences of all other Niño indices for each Niño region. In the conditioning process, we include the Trans-Niño index (TNI), which is not itself a region. Because we mask out TNI influences in this analysis, the results are independent of whether a CP El Niño or an EP El Niño currently prevails. We again create CENs for all grid points for the 1982-2021, 1982-2001, and 2002-2021 periods. We also look at causal maps for 1982-2021 with and without instantaneous links and the associated dominant lags, as in 4.2.

**Oceanic Niño Index**

Figure 22 shows the causal maps for ONI along with the conditioned players consisting of Niño 1+2, 3, 4, and TNI. Compared to Figure 10 (ONI without conditioning), the range of influence decreases along the equator in the Central Pacific and only ranges from (0N-10N, 170W-130W). There are significantly fewer red teleconnections on the Maritime Continent in the Equatorial region that are not consistent with Figure 2. Negative precipitation anomalies are still present, however, although not as pronounced as in Figure 10. There are also significantly fewer blue teleconnections in the Southwest Pacific, Brazil, East Africa, Indian Ocean, and the (30N-20N, 80W-60W) region. It is also interesting to note the change from blue (negative $\beta \sim$ 1-5, Figure 10) to red ($\beta \sim$ 1-5, Figure 22) in a small area in Africa (10S, 30E), which is consistent with Figure 2. The Southeast Pacific (blue), Northwest Pacific (blue), U.S., Arctic Regions ($\beta \sim$ 0.1-0.2 , 100E-160E) and Russia (negative $\beta \sim$ 0.1-0.2, 70N-60N, 140E-160E) remain nearly the same despite the elimination of influences from other indices. In particular, the U.S. ($\beta \sim$ 0.1-0.4) is in agreement with Figure 2. Disregarding instantaneous links, Figures 22 (right) and 23 (right) show that the Maritime Continent, the Southeast Pacific, and the largest correlating region in the Central Pacific lose many teleconnections. All other regions with lag 0 experience causal influences from ONI at least one month later.

Figures 24 and shows the causal maps for the periods 1982-2001 and 2002-2021. Compared to Figure 10, it is difficult to draw conclusions about the evolution of teleconnections because there are hardly any stable regions. It is interesting to note that the 1982-2001 period in Asia hardly changes compared to Figure 11 (left), while the Central Pacific almost disappears. The 2002-2021 period (Figure 24, right) shows signs of drought over Australia for the first time, consistent with Figure 2 and very rarely detected in all our analyses, and also not shown in Figure 12 (right). Also, we can see some red teleconnections over South America and the U.S., which can be seen in Figure 12 (right). The region east of Canada is even more magnified in Figure 24 (right) compared to Figure 12 (right), with values in the range $\beta \sim$ 0.2-5.
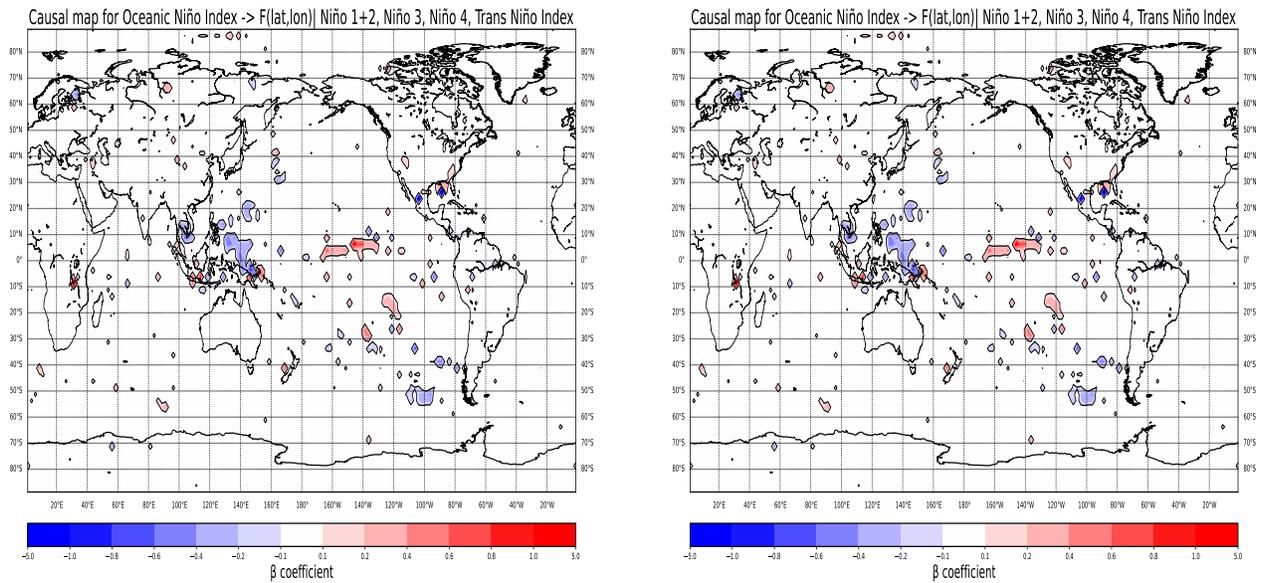
Fig 22: Left: Maximum absolute $\beta$ coefficients for the link ONI $\rightarrow$ PrecipAnom(lat,lon) for lags 0-12 (ONI runs ahead in time plus instantaneous links) obtained from PCMCI followed by standardized multiple linear regression. The trained time period is 1982-2021 (471 months). The "|" denotes the conditioned-out actors comprising Niño 1+2, 3, 4 and TNI. Right: Without instantaneous links.
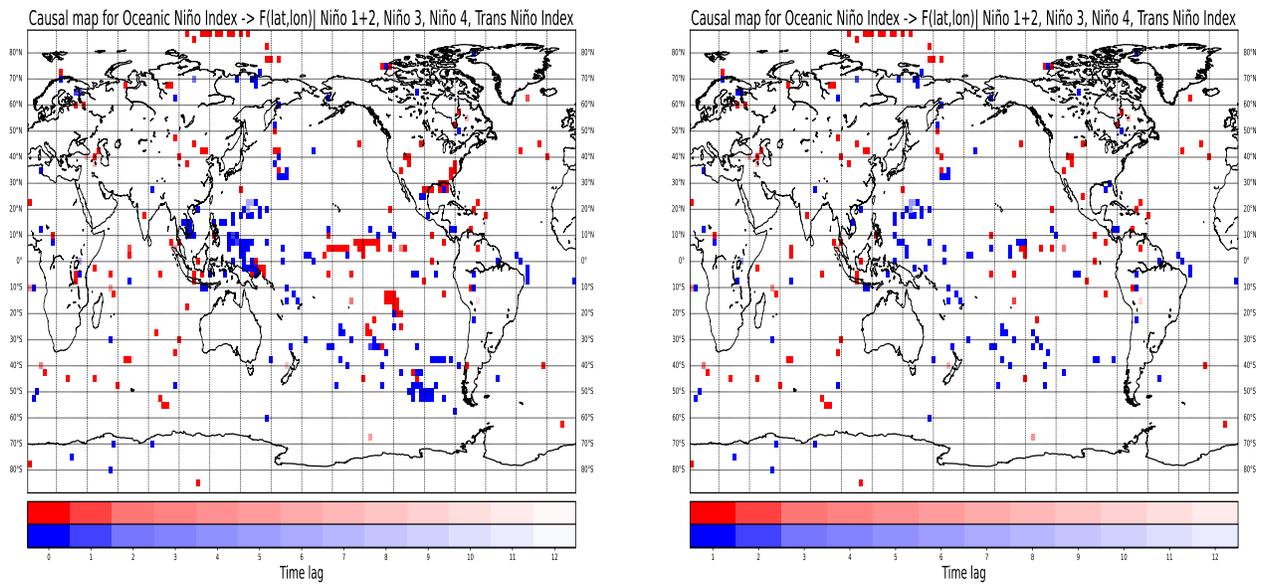


Fig 23: Left: Dominant time lags for the link ONI $\rightarrow$ PrecipAnom(lat,lon) for lags 0-10 (ONI runs ahead in time plus instantaneous links) obtained from PCMCI followed by standardized multiple linear regression. The trained time period is 1982-2021 (471 months). None of the lags 11-12 are dominant. Red dots represent $\beta_j >= 0.1$, blue dots represent $\beta_j <= -0.1$. Right: Without instantaneous links. None of the lags 11-12 are dominant.
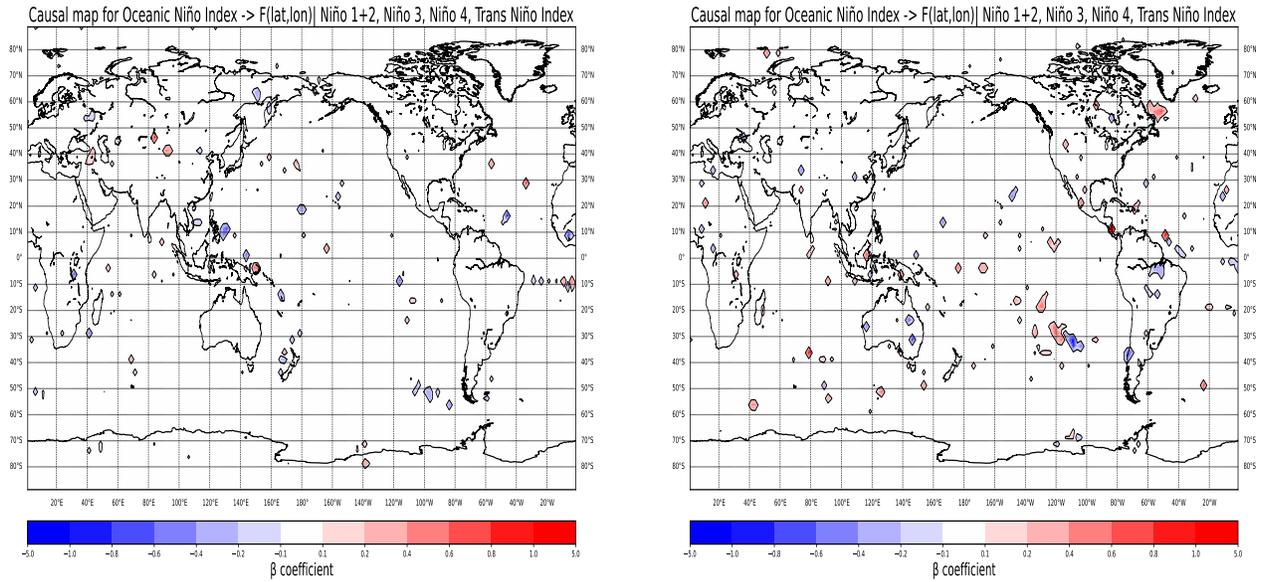
Fig 24: Left: Maximum absolute $\beta$ coefficients for the link ONI $\rightarrow$ PrecipAnom(lat,lon) for lags 0-12 (ONI runs ahead in time plus instantaneous links) obtained from PCMCI followed by standardized multiple linear regression. The trained time period is 1982-2001 (240 months). The "|" denotes the conditioned-out actors comprising Niño 1+2, 3, 4 and TNI. None of the lags 3-5 & 8-12 are dominant. Right: Maximum absolute $\beta$ coefficients for the link ONI $\rightarrow$ PrecipAnom(lat,lon) for lags 0-12 (ONI runs ahead in time plus instantaneous links) obtained from PCMCI followed by standardized multiple linear regression. The trained time period is 2002-2021 (231 months). The "|" denotes the conditioned-out actors comprising Niño 1+2, 3, 4 and TNI. None of the lags 3-4 & 6-12 are dominant.

**Niño 1+2 Index**

Next, we consider the causal maps from Figures 25-26 and compare them to the case without PCMCI conditioning. In Figure 25, the range of unexpected negative precipitation anomalies in the Central Pacific for Niño 1+2 decreases significantly when the influences of actors Niño 3, 4, ONI, and TNI are eliminated. These beta coefficients (negative $\beta \sim 0.4$-5) do not start until 130W and extend to the coast of Ecuador and Peru. This is not consistent with the rainfall patterns from Figure 2.

Likewise, most of the teleconnections in the Maritime Continent region (blue and red), as well as in the (50S-60S, 100W-80W) region (especially red), disappear during the elimination process. In the Maritime Continent (Figures 25 and 26), some positive precipitation anomalies (not consistent with Figure 2) are observed west of Java Island after conditioning ($\beta \sim 0.1$-0.2), but also in Western Australia in the range (negative $\beta \sim 0.1$-0.4) (in contrast to Figures 13 and 14), which is partially consistent with Figure 2. In particular, more red teleconnections are seen in the Western United States ($\beta \sim 0.1$-0.2) in the potentially more restrictive causal maps (Figures 25-26), consistent with Figure 2. Furthermore, we detect positive precipitation anomalies in Central Asia, southern India, the southern region of the African continent (negative $\beta \sim 0.2$-0.4). Also, teleconnections (both

red and blue, $\beta \sim 0.1\text{-}0.4$) over mainland South America are consistent with Figure 2. Omitting the instantaneous links, the positive precipitation anomalies in the Central Pacific also disappear in Figure 25 (left) compared to Figure 13 (left). Globally, lags 0 for Figure 26 (left) and lags 1 for Figure 26 (right) dominate in the causal maps.

A look at Figure 27 shows a similar reduction in negative precipitation anomalies in the Central Pacific for the 1982-2001 period as for the 1982-2021 period. Figure 15 (right) shows the expected teleconnections in the equatorial region for the 2002-2021 period in the western Central Pacific from Figure 2. These disappear in Figure 27 (right) after the influences of the other Nino indices are removed. The Maritime Continent is hardly affected by teleconnections in both Figure 27 (left and right). Of interest, as with ONI, are the positive precipitation anomalies in eastern Canada ($\beta \sim 0.2\text{-}0.6$, 60-50N, 60-40W, not visible in Figure 2) for 2002-2021. South America forms the only stable region in the (10N-0N, 60W-40) region with negative $\beta \sim 0.1\text{-}0.4$. No trend in precipitation teleconnections can be seen in the other regions. Overall, the Niño 1+2 region performs significantly worse compared to ONI in the ENSO teleconnections from Figure 2, as expected.
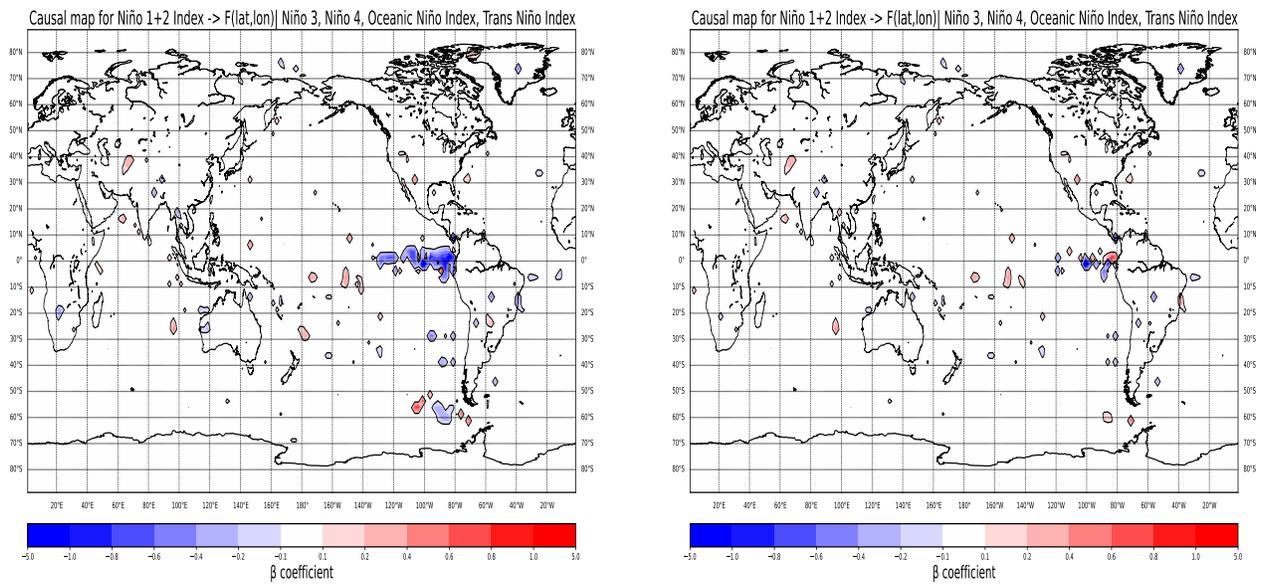


Fig 25: Left: Maximum absolute $\beta$ coefficients for the link Niño 1+2 $\rightarrow$ PrecipAnom(lat,lon) for lags 0-12 (Niño 1+2 runs ahead in time plus instantaneous links) obtained from PCMCI followed by standardized multiple linear regression. The trained time period is 1982-2021 (471 months). The "|" denotes the conditioned-out actors comprising Niño 3, 4, ONI and TNI. Right: Without instantaneous links.
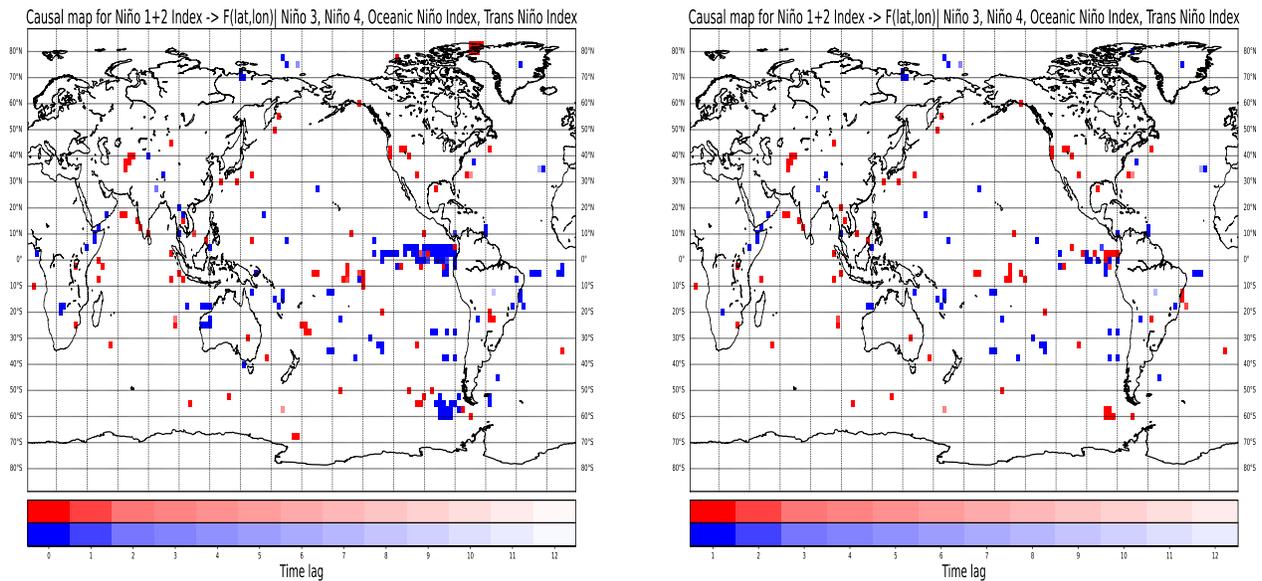
Fig 26: Left: Dominant time lags for the link Niño 1+2 → PrecipAnom(lat,lon) for lags 0-10 (Niño 1+2 runs ahead in time plus instantaneous links) obtained from PCMCI followed by standardized multiple linear regression. The trained time period is 1982-2021 (471 months). The "|" denotes the conditioned-out actors comprising Niño 3, 4, ONI and TNI. None of the lags 11-12 are dominant. Red dots represent $\beta_j >= 0.1$, blue dots represent $\beta_j <= -0.1$. Right: Without instantaneous links. None of the lags 11-12 are dominant.
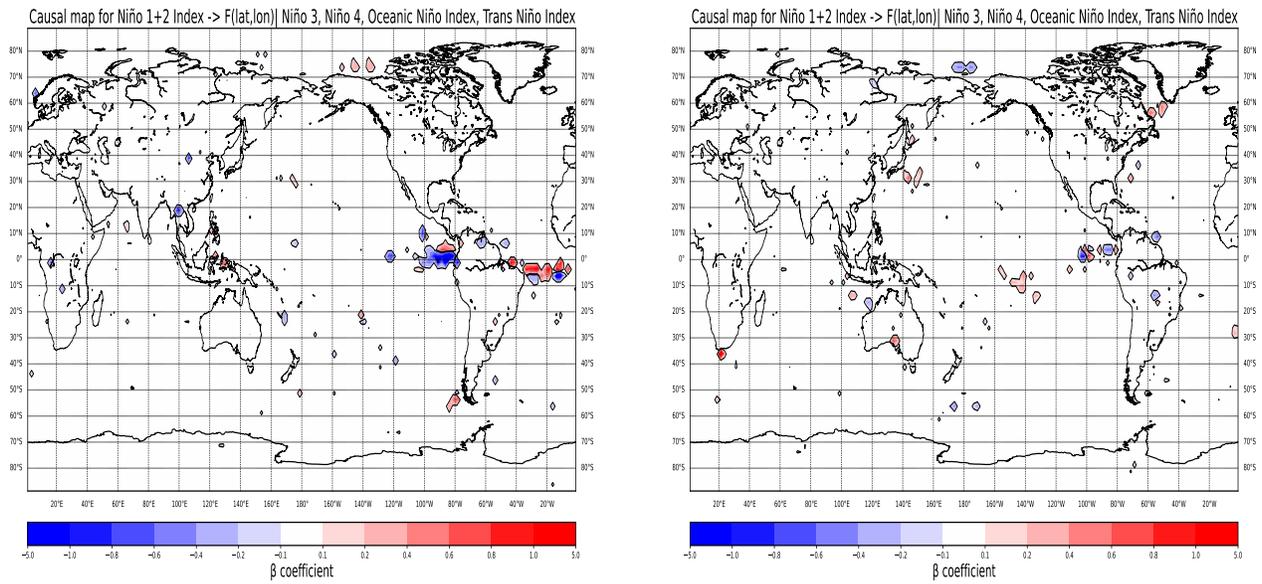
Fig 27: Left: Maximum absolute $\beta$ coefficients for the link Niño 1+2 $\rightarrow$ PrecipAnom(lat,lon) for lags 0-12 (Niño 1+2 runs ahead in time plus instantaneous links) obtained from PCMCI followed by standardized multiple linear regression. The trained time period is 1982-2001 (240 months). The "|" denotes the conditioned-out actors comprising Niño 3, 4, ONI and TNI. None of the lags 1, 3, 8, & 11-12 are dominant. Right: Maximum absolute $\beta$ coefficients for the link ONI $\rightarrow$ PrecipAnom(lat,lon) for lags 0-12 (Niño 1+2 runs ahead in time plus instantaneous links) obtained from PCMCI followed by standardized multiple linear regression. The trained time period is 2002-2021 (231 months). The "|" denotes the conditioned-out actors comprising Niño 3, 4, ONI and TNI. None of the lags 7, 9 & 11-12 are dominant.

**Niño 3 Index**

Figures 28 shows the causal maps of Niño 3 without the influences of Niño 1+2, 4, ONI, and TNI for the period 1982-2021. In the Central Pacific, it can be seen that in Figure 28, in contrast to Figure 16, the influence terminates at 150W. This is exactly the westernmost boundary of the Niño 3 region. Similar to the PCMCI case without conditioning, negative precipitation anomalies are more likely to be found north of the equatorial belt, which is not consistent with Figure 2. These blue teleconnections with negative $\beta \sim 0.1$-5 extend to 120W, the easternmost boundary of the Niño 3.4 region, see Figures 28 and 29. The remaining regions in the Central Pacific near the Equator are red ($\beta \sim 0.1$-5), as expected, but do not extend to the coast of Ecuador (as in Figure 16 and 17), with the exception of one grid point, as shown in Figure 29.

The Maritime Continent loses the most blue teleconnections when controlling for other Niño indices, see Figures 16 and 17. In contrast, many positive precipitation anomalies are preserved near the equator, especially in the (0S-10S,140E-150E) region ($\beta \sim 0.2$-5), which is not in accordance with Figure 2. Furthermore, if we compare the teleconnections in the Maritime Continent for ONI from Figures 22-23, we can see why the Nino 3.4 region is better suited for predicting droughts in these regions compared to the Niño 3 region. In comparison, the Niño 3 region performs much better for predicting droughts in Southern Africa, see Figure 29 (negative $\beta \sim 0.1$-0.2), which is consistent with Figure 2. For red teleconnections, ONI performs better than Niño 3 in the United States (particularly in the southeast), while in South America, contrary to expectations, few teleconnections are apparent for both ONI and Niño 3 compared to Figure 2, although the few marked grid points are largely consistent with Figure 2 in both cases. In particular, compared to PCMCI without conditioning, many blue teleconnections disappear in the area (50-60S, 110W-70W), while red teleconnections are lost in the USA. Some teleconnections disappear in South America, especially around 10S. In contrast, the African continent shows more negative precipitation anomalies. Compared to Figure 29 (left), the case without instantaneous connections from Figure 29 (right) has almost no blue teleconnections in the region (20S-40S, 110W-90W) and much less positive precipitation anomalies in the Central Pacific. All other regions with lag 0 as the dominant lag are noticeable in the corresponding regions at least one month later. As with the other indices, the smallest lags, i.e., lag 0 and lag 1, dominate Figure 29 (left and right), respectively.

If we look at Figure 30 (periods 1982-2001 and 2002-2021), we see that there are almost no stable regions except for the Central Pacific, where the largest correlating area is located. Interestingly, Figure 30 has only red teleconnections in the Central Pacific, which is consistent with Figure 2. The other stable region with negative precipitation anomalies is found in the southeast Pacific. The positive precipitation anomalies end around 90W in both periods, which is the easternmost boundary of the Niño 3 region.

The Maritime Continent, on the other hand, is freed from many teleconnections compared to Figure 18 (left and right), except for (10N-5S, 130E-150E, positive and negative $\beta \sim 1$-5) and some red teleconnections along the equator in Figure 30 (left). Also of interest are negative precipitation anomalies in the range (80N-70N, 160W-100W, negative $\beta \sim 0.1$-5) in Figure 30, which can already be observed for Figure 18 (left). In Figure 30 (right), as in Figure 18 (right), red teleconnections are still visible in eastern Canada, but this time in the range $\beta \sim 0.1$-1. No trends in precipitation anomalies can be observed globally.
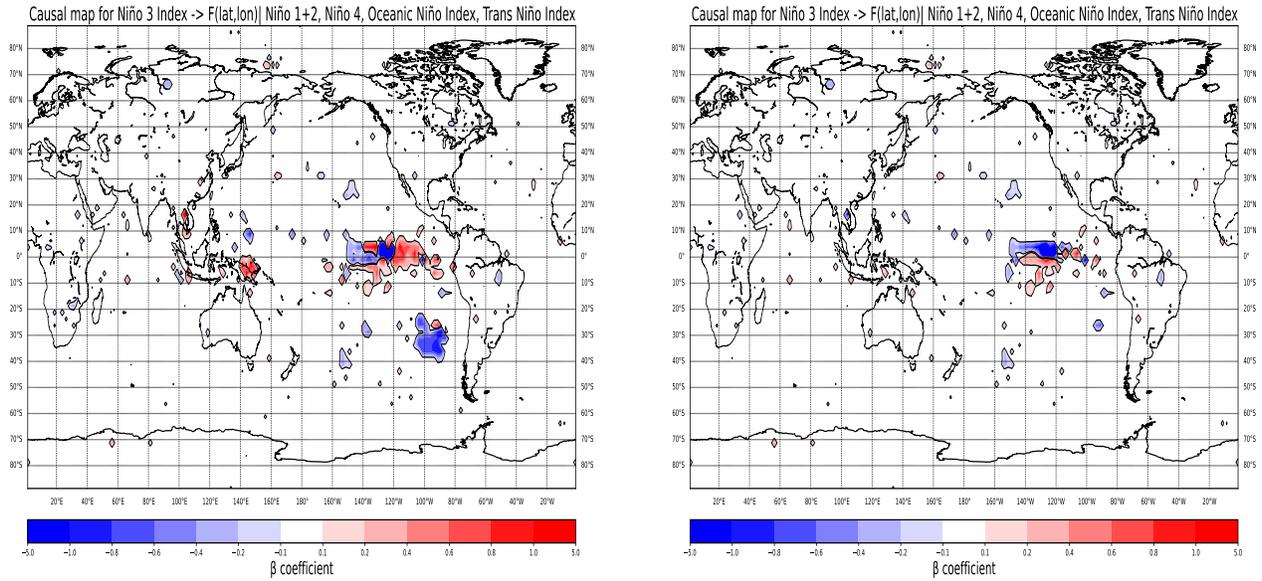
Fig 28: Left: Maximum absolute $\beta$ coefficients for the link Niño 3 $\rightarrow$ PrecipAnom(lat,lon) for lags 0-12 (Niño 3 runs ahead in time plus instantaneous links) obtained from PCMCI followed by standardized multiple linear regression. The trained time period is 1982-2021 (471 months). The "|" denotes the conditioned-out actors comprising Niño 1+2, 4, ONI and TNI. Right: Without instantaneous links.
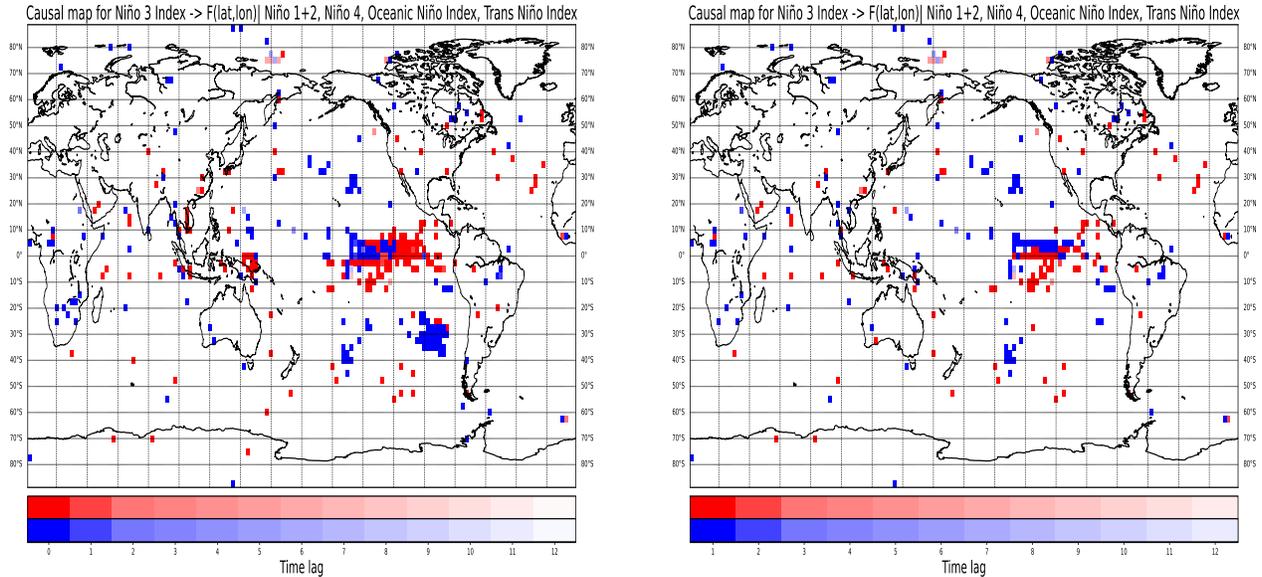


Fig 29: Left: Maximum absolute $\beta$ coefficients for the link Niño 3 $\rightarrow$ PrecipAnom(lat,lon) for lags 1-12 (Niño 3 runs ahead in time) obtained from PCMCI followed by standardized multiple linear regression. The trained time period is 1982-2021 (471 months). The "|" denotes the conditioned-out actors comprising Niño 1+2, 4, ONI and TNI. Right: Without instantaneous links. None of the lags 9-12 are dominant.
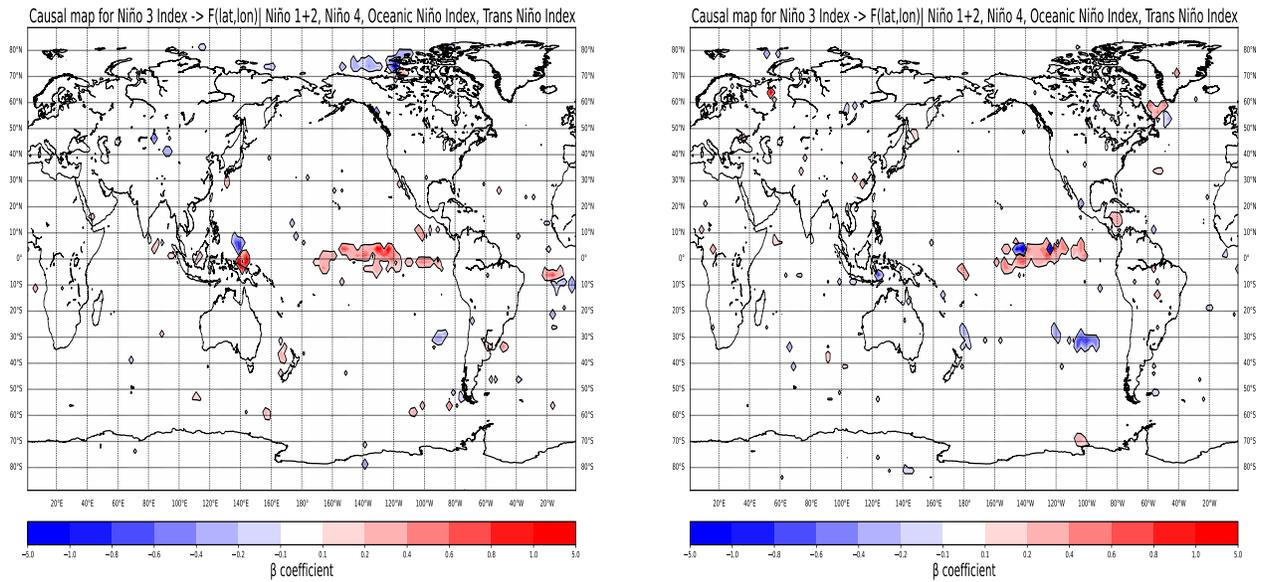
Fig 30: Left: Maximum absolute $\beta$ coefficients for the link Niño 3 $\rightarrow$ PrecipAnom(lat,lon) for lags 0-12 (Niño 3 runs ahead in time plus instantaneous links) obtained from PCMCI followed by standardized multiple linear regression. The trained time period is 1982-2001 (240 months). The "|" denotes the conditioned-out actors comprising Niño 1+2, 4, ONI and TNI. None of the lags 2, 6-8 & 10-12 are dominant. Right: Maximum absolute $\beta$ coefficients for the link Niño 3 $\rightarrow$ PrecipAnom(lat,lon) for lags 0-12 (Niño 3 runs ahead in time plus instantaneous links) obtained from PCMCI followed by standardized multiple linear regression. The trained time period is 2002-2021 (231 months). The "|" denotes the conditioned-out actors comprising Niño 1+2, 4, ONI and TNI. None of the lags 5, 8 & 10-12 are dominant.

## Niño 4 Index

Finally, we examine the role of the Niño 4 index for the periods 1982-2021 (Figures 31-32), 1982-2001 and 2002-2021 (Figure 33) by conditioning on Niño 1+2, 3, ONI, and TNI. Compared to Figure 19 in the 1982-2021 period (PCMCI without conditioning), the Central Pacific in the equatorial region from Figure 31 has slightly fewer red teleconnections ($\beta \sim$ 0.2-5) up to 150W (easternmost boundary of the Niño 4 region). Nevertheless, a few red as well as unexpected blue teleconnections exist eastward outside the Niño 4 region, see Figure 32.

The Maritime Continent also has fewer negative precipitation anomalies (negative $\beta \sim$ 0.2-5) in Figures 31 and 32, but many red precipitation anomalies disappear, especially in western Indonesia, which are not compatible with Figure 2. The Southwest Pacific region (negative $\beta \sim$ 0.2-5) remains largely unaffected by conditioning except for (30S-40S, 170W). Furthermore, red teleconnections in Asia ($\beta \sim$ 0.2-5), as well as blue teleconnections in northeast Brazil (negative $\beta \sim$ 0.4-5), which are consistent with Figure 2, are preserved. In addition, some blue teleconnections around 10S continue to be seen on the west coast of South America, consistent with Figure 2 (negative $\beta \sim$ 0.1-0.4). Meanwhile, the area between the Dominican Republic, Puerto Rico, and Venezuela shows positive precipitation anomalies with beta coeffients $\beta \sim$ 0.1-0.4.

Other regions that are largely preserved but not consistent with Figure 2 include the Atlantic Ocean with many clusters of blue (negative $\beta \sim$ 0.1-0.8) and red ($\beta \sim$ 0.1-0.8) teleconnections that contain some lags in the 3-10 range, as well as Europe ($\beta \sim$ 0.1-0.2). Moreover, two blue teleconnections with negative beta coefficients $\beta \sim$ 0.1-0.2 at 60N in Russia and positive precipitation

anomalies over Italy $\beta \sim 0.1$-0.2 are interestingly observed in Europe. Also, in contrast to Figure 20 (left), two red gridpoints can be detected off the southwestern coast of India in Figure 31 ($\beta \sim$ 0.2-0.4), and we suspect that may belong to the October-December season (3 months) from Figure 2. The area around eastern Canada has already come to our attention for the Niño 1+2, 3, and ONI due to positive precipitation anomalies, but for the 2002-2021 time window. We see red teleconnections in the $\beta \sim 0.1$-5 range for Figure 31 (1982-2021 period).

In the Pacific Ocean, we also see some blue teleconnections in the Bering Sea region (negative $\beta \sim$) 0.1-5, in the (30N-20N, 170W-150W) region negative precipitation anomalies (negative $\beta \sim$ 0.2-5), and in the (50S, 150W-130W) region positive precipitation anomalies ($\beta \sim 0.1$-1). In the U.S., there are both blue and red regions in the range $\beta \sim 0.1$-0.2 compared to PCMCI without conditioning. Omitting lag 0 results in Figures 31 (right) and 32 (right), where the Maritime Continent around the Phillipines changes from blue (lag 0) to red (lag 1) ($\beta \sim 0.1$-5) compared to Figure 32. In addition, red teleconnections disappear in eastern Canada and the north (blue) and south Central Pacific (red). All other marked regions with lag 0 as the dominant lag experience influences from the Niño 4 region at least one month later. Comparing the predictive power of Niño 4 (Figures 31 and 32) with ONI (Figures 22 and 23) using Figure 2, we find that South America, Central Asia, the Phillipines in the Maritime Continent, and the north Central Pacific have more clusters of teleconnections in agreement with Figure 2.

Figure 33 shows the 1982-2001 and 2002-2021 periods, respectively. With the exception of some areas of the Central Pacific around the equator, there are virtually no stable regions. In the Maritime Continent, there are more blue dots in the number of teleconnections in the 1982-2001 period than in the 2002-2021 period, while the number of red regions that do not match Figure 2 is increasing (see Figure 33, right). It is also interesting that Figure 33 (left) predicts droughts (negative $\beta \sim$ 0.1-0.4) in northeastern Brazil according to Figure 2, while there are no blue teleconnections in Figure 33 (right). On the other hand, precipitation patterns for the Chilean coast ($\beta \sim 0.1$-0.4) are consistent with Figure 2 for the period 2002-2021. Central Asia is also covered by Figure 33 (right) of red teleconnections in the range $\beta \sim 0.1$-0.4, which we find in Figure 2. In addition, negative precipitation anomalies are observed in the Arctic regions (negative $\beta \sim 0.1$-0.4) and in the Bering Sea ($\beta \sim 1$-5) in Figure 33 (left), while many red teleconnections are found in the north off the South American coast and in the North Atlantic ($\beta \sim 0.2$-5) and in the Antarctic region ($\beta \sim$ 0.2-0.6) in Figure 33 (right). Also of note is a region in the north Central Pacific (30N-20N,150W) with beta coefficients (negative $\beta \sim 1$-5). Other than the fact that there are slightly fewer blue teleconnections in Figure 33 (right) than in Figure 33 (left), no trends in precipitation anomalies are apparent.
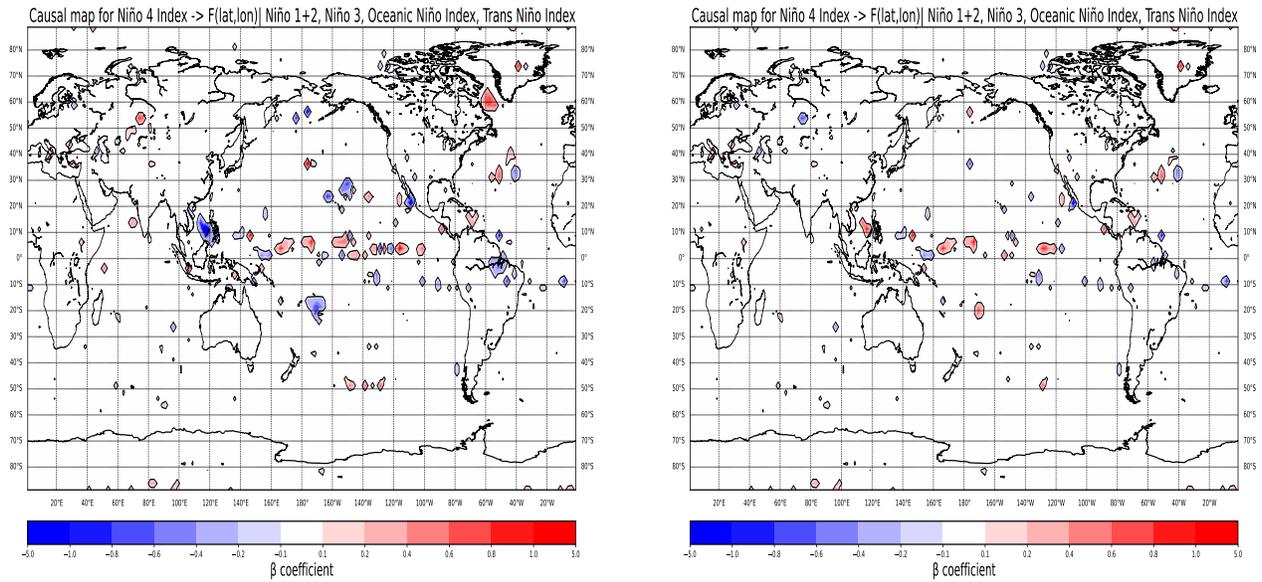
Fig 31: Left: Maximum absolute $\beta$ coefficients for the link Niño 4 $\rightarrow$ PrecipAnom(lat,lon) for lags 0-12 (Niño 4 runs ahead in time plus instantaneous links) obtained from PCMCI followed by standardized multiple linear regression. The trained time period is 1982-2021 (471 months). The "|" denotes the conditioned-out actors comprising Niño 1+2, 3, ONI and TNI. Right: Without instantaneous links.
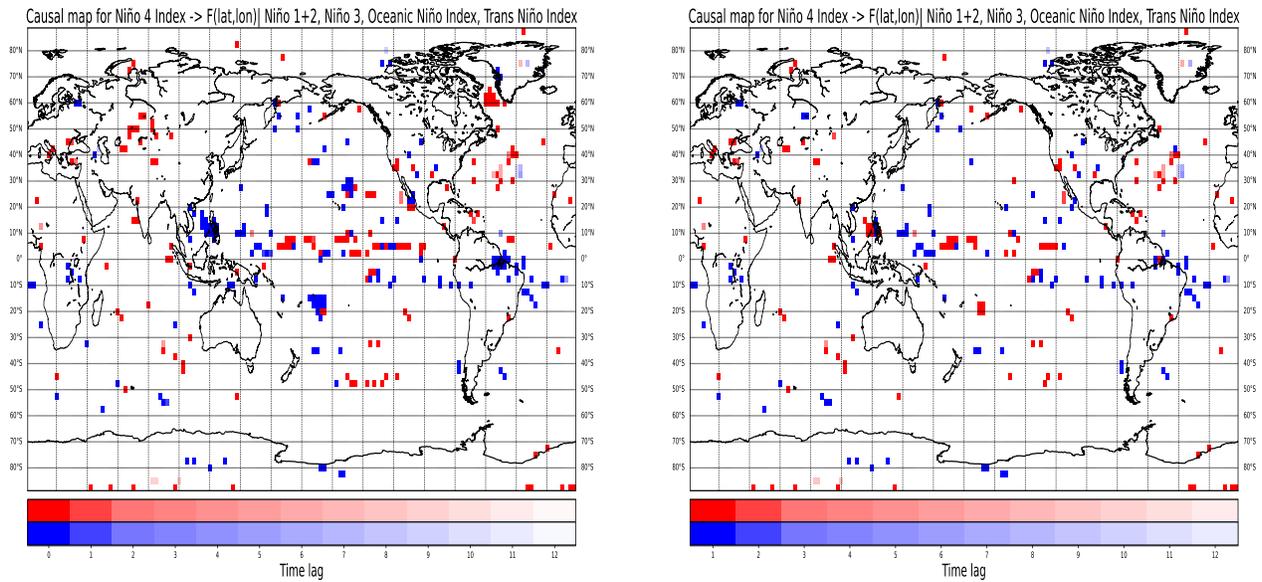


Fig 32: Left: Dominant time lags for the link Niño 4 $\rightarrow$ PrecipAnom(lat,lon) for lags 0-10 (Niño 4 runs ahead in time plus instantaneous links) obtained from PCMCI followed by standardized multiple linear regression. The trained time period is 1982-2021 (471 months). The "|" denotes the conditioned-out actors comprising Niño 1+2, 3, ONI and TNI. None of the lags 11-12 are dominant. Red dots represent $\beta_j >= 0.1$, blue dots represent $\beta_j <= -0.1$. Right: Without instantaneous links. None of the lags 11-12 are dominant.
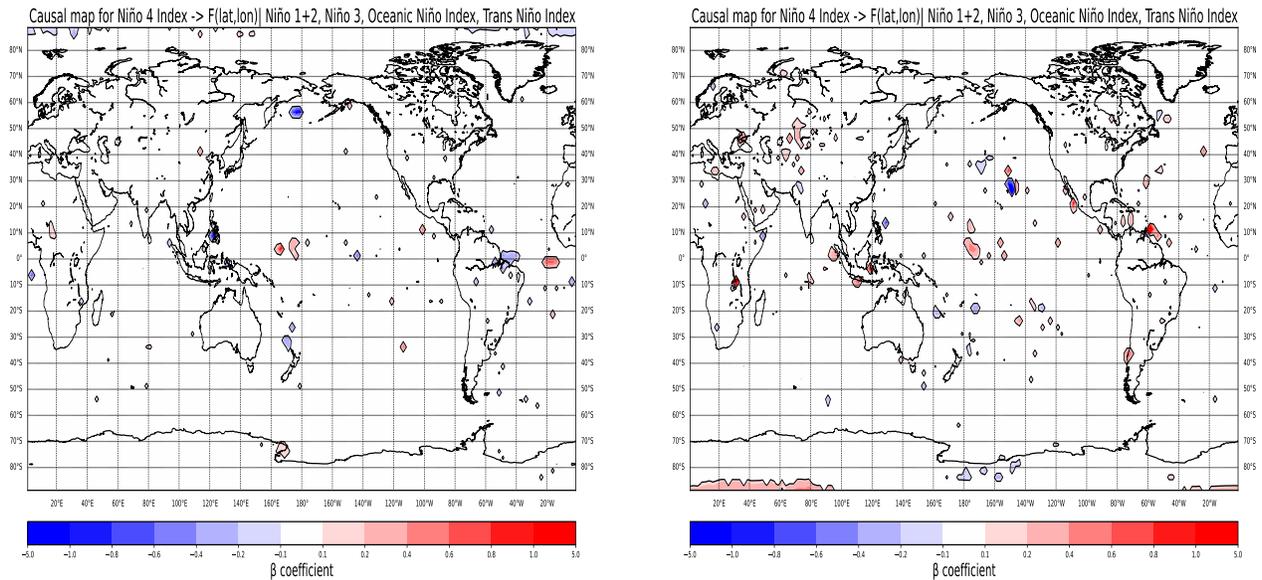
Fig 33: Left: Maximum absolute $\beta$ coefficients for the link Niño 4 $\rightarrow$ PrecipAnom(lat,lon) for lags 0-12 (Niño 4 runs ahead in time plus instantaneous links) obtained from PCMCI followed by standardized multiple linear regression. The trained time period is 1982-2001 (240 months). The "|" denotes the conditioned-out actors comprising Niño 1+2, 3, ONI and TNI. None of the lags 2-4, 8 & 11-12 are dominant. Right: Maximum absolute $\beta$ coefficients for the link Niño 4 $\rightarrow$ PrecipAnom(lat,lon) for lags 0-12 (Niño 4 runs ahead in time plus instantaneous links) obtained from PCMCI followed by standardized multiple linear regression. The trained time period is 2002-2021 (231 months). The "|" denotes the conditioned-out actors comprising Niño 1+2, 3, ONI and TNI. None of the lags 3, 8 & 10-12 are dominant.

## 4.4 Additional remarks and recommendations

In the first part of the correlation analysis, we identified and quantified the largest correlating and anticorrelating areas for ONI. In doing so, we found a positive precipitation anomaly in the tropical Pacific, while the Maritime Continent & Southwest Pacific regions are affected by droughts. This is consistent with Figure 2. It is particularly interesting to note how the Maritime Continent & Southwest Pacific region has decreased from the maximum extent in the first window [1979, 1988] of 11, 757, 936 $km^2$ to 2, 931, 376 $km^2$ in the last window [2012, 2021]. In contrast, the largest correlating area in the tropical Pacific is much more stable, with a maximum extent in the [1991, 2000] time window of 9, 402, 819 $km^2$ and the smallest area also in the [2012, 2021] time window of 6, 158, 208 $km^2$. The results of Figure 2 show that the influences of ENSO on precipitation and drought have an oscillating character in terms of area, but decrease overall. In particular, in the Maritime Continent & Southwest Pacific region, the area of regions with significant drought decreases sharply. We know that very strong El Niño events (1982-1983, 1997-1998, 2015-2016) are classified as such when three consecutive months have ONI values of at least ONI $>= 2$ (Golden GateWeather Services, 2022, availabe at https://ggweather.com/enso/oni.htm, last access: 28 February 2022). We see that the 1984 and 1997 time windows in Figure 3 have increased area just when strong El Niño events are present. Surprisingly, the 2015-2016 El Niño does not appear to have caused a large increase in area in the Maritime Continent & Southwest Pacific Region and the tropical Pacific. Also, relatively large teleconnection areas can be observed

40

during strong La Niña events (1988-1989, 1999-2001, 2010-2011).

The results suggest a decreasing influence of ENSO on precipitation in the most influential areas and raise the question of the extent to which climate change plays a role, possibly related to a weakening or even strengthening of the Walker circulation (Power et al., 2007; Zhao et al., 2019). However, the results do not tell us anything about changes in ENSO-related precipitation teleconnections in specific months. For example, the strongest El Niño and La Niña events tend to occur in October through February (Golden Gate Weather Services, 2022). Further correlation studies should consider specific monthly periods, quantify the largest regions occurring there, and plot their temporal trends. It would even be appropriate to conduct local and seasonal analyses under higher temporal resolution (for example, half-monthly or quater-monthly). The problem with this approach is that the SSTs and corresponding indices in the Pacific are based on monthly averages. It is hoped that similar analyses will be conducted on temperature anomalies associated with ENSO.

Similar considerations can be made when examining the dominant lags from the second part of the correlation analysis. Nevertheless, the fact that the Niño indices are highly correlated with each other is evident from 4.1.2. Therefore, as we saw in the sections on PCMCI+CEN, the results cannot necessarily be considered representative of the Niño index. Nevertheless, expert knowledge of the superior predictive power of the Niño 3.4 and 4 regions compared to Niño 1+2 can be used to describe phenomena that occur in the context of ENSO without the need to include confounding variables in the analyses. As a result, a simple correlation analysis may suffice. The consistency of dominant lags indicates that in the range $\tau_{min} = -1$ to $\tau_{max} = -12$ (month) Niño region independent lags $\tau_{min} = -1$ (month) globally dominate most grid points related to ENSO. This observation can be confirmed with PCMCI+CEN with and without conditioning, although the causal maps without instantaneous links ($\tau_{min} = 0$) deviate strongly in some cases from the correlation analysis of 4.1.2. This could be partly due to the fact that in 4.1.2 we consider 10-year moving windows over the period 1982-2021, while in PCMCI+CEN we compute partial correlations over the entire period. This illustrates one of the problems we observe with 4.2 and 4.3, respectively. Short periods such as 1982-2001 (240 months) and 2002-2021 (231 months) contain much less information and are associated with more noise. It follows that it is difficult to draw conclusions about the evolution of teleconnections. Further studies should consider higher time resolutions (daily or weekly) or longer time periods, for example, to combine PCMCI+CEN with sliding time windows. The similarity of the results from 4.1.2 with sliding time windows from 4.1.1 as well as Figure 2 implies large autocorrelations of ENSO indices (Sajani Surendran et. al., 2015). Therefore, PCMCI+CEN offers itself as an alternative when there is a large intercorrelation between potential actors and additionally high autocorrelations.

Moreover, following the example of causal maps (Di Capua et al., 2020), we further extended the causal maps by extracting for each grid point the time lag that has the largest absolute beta coefficient. In this way, in addition to causal strenghts of particular teleconnetion origins, we can assess which specific time lag causes precipitation anomalies. Excluding instantaneous links, lag 1 ($\tau_{min} = -1$) consistently emerges as the dominant leading lag for all causal maps over the 1982-2021 period (471 months). This is consistent with the second part of the correlation analysis from 4.1.2. When considering instantaneous connections ($\tau_{min} = 0$), lag 0 always wins (for the majority of teleconnections) in all causal maps for 1982-2021 (471 months). Overall, when moving from PCMCI without conditioning to the elimination of confounding variables (Niño regions), it can be seen that a reduction in teleconnections occurs. Nevertheless, a few regions appear in PCMCI

with conditioning that are not visible in PCMCI without conditioning, which is due to suppressor variables. The largest reductions in teleconnections after PCMCI with conditioning is introduced are found for the Niño 3 region. The other regions Niño 1+2, 4, and ONI lose approximately the same number of teleconnections. Interestingly, the Niño 4 region performs better (1982-2021) than ONI in some regions in the PCMCI+CEN analyses when comparing both indexes to the ENSO-associated regions from Figure 2. These include South America (Brazil on the Amazon), Central Asia, the Phillipines on the Maritime Continent, and the north Central Pacific. In comparison, the ONI has better (1982-2021) predictive power for positive precipitation anomalies in the U.S. and also has slightly more blue teleconnections over the Maritime Continent. Niño 3, on the other hand, performs better (1982-2021) in predicting droughts in the southern part of the African continent and rainfall patterns in the region (35N-10N, 105E-130E) that includes parts of southern Japan and eastern China. In predicting droughts, the Niño 1+2 region performs well in South Africa, Western Australia, and the east coast of South America. Central Asia and the west coast of the USA with forecasts for precipitation are also accurate according to Figure 2 (1982-2021). Surprisingly, predictions for positive precipitation anomalies in the Central Pacific for the range (160E-160W) turn out to be sporadic for all Niño regions, in contrast to correlation analysis 4.1.1. In addition, PCMCI+CEN lacks teleconnections for the Darién gap, which are always associated with the negative precipitation anomaly in 4.1.1.

At this point, it should be explicitly mentioned again that the causal interpretations of PCMCI+CEN come with some assumptions, such as stationarity, linear relationships between variables, causal Markov condition, or unconfoundedness. Of course, there may be other actors that play a crucial role as common drivers (Di Capua et al., 2020). For more information on the assumptions of causal discoveries in Earth systems and PCMCI, we refer to Runge et al., 2019.

## 5 Conclusion

In our analyses, we find teleconnection patterns for rainfall and drought for different Niño regions (Niño 1+2, 3, 4 and ONI) under different conditions, and compare them with the current knowledge of ENSO from the International Research Institue for Climate and Society (IRI) from Figure 2. To do this, we look at the monthly precipitation anomalies for 10368 grid points (2.5° x 2.5°) worldwide, while simultaneously observing the monthly SST anomalies for the different Niño regions in the equatorial Pacific. The goal is to identify the evolution of ENSO-specific precipitation patterns, to assign precipitation teleconnections to Niño regions and their preceding time lags, and to identify stable and less stable regions. In addition, we compare the predictive power of the different Niño regions with each other. Our main tools are the correlation analysis and the PCMCI+CEN approach. In all our analyses, we use a significance level of $\alpha = 0.05$ and the Benjamini-Hochberg method to avoid the problem of multiple testing.

In the first part of our analysis, we examine 10-year time windows for the Oceanic Niño Index (ONI) from the Niño 3.4 region (5N-5S, 170W-120W) during the period 1979 to March 2021. The most stable and largest regions across time windows are the Maritime Continent & Southwest Pacific and the Central Pacific in the tropics, which are confirmed with a correlation analysis without time lags. These results are consistent with Figure 2. The Maritime Continent & Southwest Pacific Region experience enhanced droughts during an El Niño episode due to a shift of the rising branch of the Walker circulation toward the tropical Central Pacific. The largest extent of significant ENSO anticorrelation area is found in the 10-year time window $[1979, 1988]$ and is $11,757,936$

$km^2$. The smallest extent is found in the most recent time window $[2012, 2021]$ and is $2,931,376$ $km^2$, while the average area of all 34 time windows is $7,684,786\ km^2$. Overall, the Maritime Continent & Southwest Pacific region is experiencing a decrease in drought areas associated with a positive ONI values. In the tropical Pacific, the rising branch of the Walker circulation is found in the El Niño case, and the significant area of positive precipitation anomalies is $9,492,819\ km^2$ in time window $[1991, 2000]$. The smallest extent of positive precipitation anomalies is found in the last time window with $6,158,208\ km^2$, while the average area is $6,158,207\ km^2$. In the tropical Pacific, as in the Maritime Continent & Southwest Pacific region, a decreasing trend of significant areas is observed, but not as strong, such that a smaller elongation exists (see Figure 3). Other stable regions found in all 34 windows are in the northern part of the South American continent, which includes the Darien Gap and the northern part of Brazil, and are associated with droughts at positive ONI values. Many other areas, including regions in Africa, Central Asia, and the United States, can be verified in agreement with Figure 2, but only in specific time periods.

In the second part of the correlation analysis, we look at 31 10-year sliding windows over the period 1982-2021 for Niño 1+2 , 3, 4 and ONI. We always get $\tau = -1$ as dominant lags for lags in the range $\tau_{min} = -1$ and $\tau_{max} = -12$ for the medians and modes. This is true for all Niño regions, with all the indexes running monthly ahead in time as they are assumed to cause precipitation anomalies. Here, the regions showing dominant lags are consistent with Figure 2 except for (40N-30N, 40E-50E, Niño 3). However, autocorrelations as well as intercorrelations (common drivers & indirect links) of the Niño regions can make results difficult to interpret.

In this context, CENs constructed with PCMCI can remedy the situation by counteracting ambiguities in correlation analyses. This involves finding areas with precipitation anomalies that can be assigned to specific Niño regions (Niño 1+2, 3, 4, and ONI). As with the correlation analysis for $\tau_{min} = -1$ and $\tau_{max} = -12$ in the PCMCI studies, $\tau = -1$ also prevailed as the dominant lag for all Niño regions. If $\tau_{min} = 0$ is then added (instantenous links), lag 0 wins with the absolute largest beta coefficients ($\beta_j$ from standardized multiple regression after the MCI step) for most teleconnections.

The Niño 1+2 region proved successful in predicting teleconnections from Figure 2 after eliminating the influences of Niño 3,4 and ONI, particularly in southern Africa (drought), Central Asia (precipitation), Western Australia (drought), and some areas of the United States (precipitation). Niño 3 influences shows up in the area of southern Japan and eastern China (precipitation), southern Africa (drought), and precipitation in the tropical Pacific (0S-15S, 140W-120W & 10N-5S, 120W-90W), which is consistent with Figure 2. The ONI has the greatest predictive power for the Maritime Continent and the Southwestern Pacific region (drought), the United States (precipitation), and some areas in Central America (drought). In contrast, the Niño 4 region performs particularly well in Central Asia (precipitation), over the Philippines (drought), Brazil (drought), and in the Pacific (10N-0N, precipitation).

The results of the correlation analyses may motivate a closer look at the diminishing influences of ENSO in the Maritime Continent & Southwest Pacific, as well as in the tropical Pacific. In particular, seasonal analyses with sliding windows would be of interest, such as October-February, where particularly strong El Niño and La Niña events occur. In this context, what remains to be addressed is the extent to which climate change affects ENSO, particularly with an eastward shift of the Walker circulation (Sohn et al., 2014). PCMCI+CEN results may help to better understand the causal relationships between SST values in the Central Pacific and global precipitation anomalies, especially in the context of ENSO diversity. Furthermore, it may be of great importance for

ENSO-prone regions to use specific Niño regions to predict potential precipitation or even temperature anomalies based on causal detection methods such as PCMCI. Further research should clarify whether there are explanations for the causal links between the Niño regions and the areas affected by teleconnections, and whether these findings can be used to improve precipitation or drought forecasts during ENSO.

*References*

1 Y. Benjamini and Y. Hochberg, "Controlling the false discovery rate: A practical and powerful approach to multiple testing," 289–300, Journal of the Royal Statistical Society. Series B (1995). https://doi.org/10.1111/j.2517-6161.1995.tb02031.x.

2 G. D. Capua, J. Runge, R. V. Donner, *et al.*, "Dominant patterns of interaction between the tropics and mid-latitudes in boreal summer: causal relationships and the role of timescales," 522–533, Weather and Climate Dynamics (2020). https://doi.org/10.5194/wcd-1-519-2020.

3 D. Espinoza-Morriberón, V. Echevin, F. Colas, *et al.*, "Impacts of el niño events on the peruvian upwelling system productivity," 5423, AGU Publications (2017). https://doi.org/10.1002/2016JC012439.

4 M. Kretschmer, D. Coumou, J. F. Donges, *et al.*, "Using causal effect networks to analyze different arctic drivers of midlatitude winter circulation," 4069–4081, Journal Climate (2016). https://doi.org/10.1175/JCLI-D-15-0654.1.

5 J. Runge, P. Nowack, M. Kretschmer, *et al.*, "Detecting and quantifying causal associations in large nonlinear time series datasets," 1–13, Science Advances, 5, 11, eaau4996 (2019). https://doi.org/10.1126/sciadv.aau4996.

6 K. E. Trenberth and D. P. Stepaniak, "Indices of el niño evolution," 1697–1701, Journal Climate (2001). https://doi.org/10.1175/1520-0442(2001)014¡1697:LIOENO¿2.0.CO;2.

7 H. Y. Kao and J. Y. Yu, "Contrasting eastern-pacific and central-pacific types of enso," 615–632, Journal Climate (2008). https://doi.org/10.1175/2008JCLI2309.1.

8 P. Spirtes, C. Glymour, and R. Scheines, "Causation, prediction, and search,," Boston, The MIT Press (2000).

9 B. Zogheib and A. Elsaheli, "Approximations to the t distribution," 2445 – 2449, Applied Mathematical Sciences, Vol. 9, no. 49 (2015). http://dx.doi.org/10.12988/ams.2015.52148.

10 S. Banik and B. G. Kibria, "Confidence intervals for the population correlation coefficient ," 99–111, International Journal of Statistics in Medical Research (2016). http://dx.doi.org/10.6000/1929-6029.2016.05.02.4.

11 S. B. Power and I. N. Smith, "Weakening of the walker circulation and apparent dominance of el niño both reach record levels, but has enso really changed?," 1–4, Geophysical Research Letters, VOL. 34, L18702 (2007). https://doi.org/10.1029/2007GL030854.

12 B. J. Sohn, S.-W. Yeh, J. Schmetz, *et al.*, "Observational evidences of walker circulation change over the last 30 years contrasting with gcm results," 1721–1732, Climate Dynamics (2013). https://doi.org/10.1007/s00382-012-1484-z.

13 X. Zhao and R. J. Allen, "Strengthening of the walker circulation in recent decades and the role of natural sea surface temperature variability," 1–9, Environmental Research Communications, Volume 1, Number 2 (2019). https://doi.org/10.1088/2515-7620/ab0dab.

14  M. B. Freund, B. J. Henley, D. J. Karoly, *et al.*, "Higher frequency of central pacific el niño events in recent decades relative to past centuries," 450–455, Nature Geoscience volume 12 (2019). https://doi.org/10.1038/s41561-019-0353-3.

15  W. Cai, M. J. McPhaden, A. M. Grimm, *et al.*, "Climate impacts of the el niño–southern oscillation on south america," 215–231, Nature Reviews Earth  Environment volume 1 (2020). https://doi.org/10.1038/s43017-020-0040-3.

16  T. Haszpra, M. Herein, and T. Bodai, "Prediction of indian rainfall during the summer monsoon season on the basis of links with equatorial pacific and indian ocean climate indices," 267–280, Earth System Dynamics, Volume 11, Issue 1 (2020). https://doi.org/10.5194/esd-11-267-2020.

17  W. Cai, M. J. McPhaden, A. M. Grimm, *et al.*, "Investigating enso and its teleconnections under climate change in an ensemble view - a new perspective," 215–231, Nature Reviews Earth  Environment volume 1 (2020). https://doi.org/10.1038/s43017-020-0040-3.

18  K. E. Trenberth, "Niño sst indices (niño 1+2, 3, 3.4, 4; oni and tni)," National Center for Atmospheric Research, Climate Data Guide (2016). https://climatedataguide.ucar.edu/climate-data/nino-sst-indices-nino-12-3-34-4-oni-and-tni.